Frequency analysis of pressure oscillations in large length-to-diameter two-phase micro-channel heat sinks

CrossMark

Seunghyun Lee, V.S. Devahdhanush, Issam Mudawar *

Boiling and Two-Phase Flow Laboratory (PU-BTPFL), School of Mechanical Engineering, Purdue University, 585 Purdue Mall, West Lafayette, IN 47907, USA

ABSTRACT

Two-phase micro-channel heat sinks are prime candidates for incorporation into thermal control systems (TCSs) of future space vehicles and planetary habitats. Unlike small heat sinks employed in the electronics industry, TCS heat sinks are characterized by large length-to-diameter ratio, for which limited information is presently available. This study employs a 609.6-mm long by 203.2-mm wide heat sink containing 100 of $1 \times 1 \text{ mm}^2$ micro-channels and uses R134a as working fluid. The large length-to-diameter ratio of 609.6 is especially instrumental to capturing detailed axial variations of flow pattern and corresponding variations in local heat transfer coefficient. High-speed video analysis of the inlet plenum shows appreciable vapor backflow under certain operating conditions, which is also reflected in periodic oscillations in the measured pressure drop. In fact, the backflow frequency captured by video matches closely the frequency obtained from Fourier analysis of the pressure drop signal. While density-wave oscillations are encountered in individual channels, the phenomena observed are more closely related to parallel-channel instability. It is shown the periodic oscillations and vapor backflow are responsible for initiating intermittent dryout and appreciable drop in local heat transfer coefficient in the downstream regions of the channels. A parametric study of oscillation frequency shows a dependence on four dimensionless parameters that account for amount of vapor generation, subcooling, and upstream liquid length, in addition to Weber number. A new correlation for oscillation frequency is constructed that captures the frequency variations relative to these individual parameters.

© 2017 Elsevier Ltd. All rights reserved.

1. Introduction

1.1. Emergence of Two-phase cooling technologies

During the past four decades, the rate of heat dissipation in a number of technologies, especially electronics and power applications, has increased enormously, exasperated by a quest for smaller and more lightweight system architectures. To cope with these challenges, a variety of two-phase high-heat-flux thermal management techniques, with device heat fluxes in the range of 10^2–10^3 W/cm^2, have been proposed, and some have evolved into practical solutions [1]. The most basic of these techniques are passive cooling schemes such as capillary-driven devices (heat pipes, capillary pumped loops, and loop heat pipes) [2–4] and pool boiling thermosyphons [5–7]. But the more demanding cooling situations are tackled with the aid of a mechanical pump to capitalize upon the heat transfer merits of faster fluid motion. The pumped

cooling schemes are the focus of extensive studies that have been performed at the Purdue University Boiling and Two-Phase Flow Laboratory (PU-BTPFL). They include falling film [8], channel flow boiling [9–13], mini/micro-channel flow boiling [14–20], jet-impingement [21–23], and spray [24–28], as well as hybrid cooling schemes combining the merits of mini/micro-channel flow boiling and jet impingement [29].

1.2. Two-phase mini/micro-channel cooling

As discussed in [30], mini/micro-channel flow boiling has received unprecedented attention because of its ability to not only achieve high heat fluxes, but also reduce size and weight of cooling hardware as well as coolant inventory, let alone their design simplicity and low manufacturing cost. It is important to note that single-phase mini/micro-channel heat sinks have also received significant attention, especially in the electronics industry. The primary merit of this single-phase cooling scheme is the inverse dependence of heat transfer coefficient on hydraulic diameter for laminar flow typically encountered in mini/micro-channels, meaning cooling performance may be enhanced simply by decreasing

Nomenclature

A	cross-sectional area of micro-channel [m^2]
A_{base}	total base area of heat sink [m^2]
Bo	boiling number
C_n	complex Fourier coefficient
c_p	specific heat at constant pressure [J/kg K]
D_h	hydraulic diameter [m]
f	frequency [Hz]
f_k	complex form of Fourier series
f_{margin}	marginal frequency [Hz]
$\hat{f}$	discrete Fourier transform
$\hat{f}^*$	complex conjugate of discrete Fourier transform
G	mass velocity [kg/m^2 s]
h	enthalpy [J/kg]; heat transfer coefficient [W/m^2 K]
H_{ch}	height of micro-channel's cross-section [m]
h_{fg}	latent heat of vaporization [J/kg]
$I_{sp,f}$	dimensionless single-phase liquid length parameter
j	superficial velocity [m/s]
k	thermal conductivity [W/m K]
L	micro-channel length [m]
L_H	heated length of channel [m]
m	fin parameter
$\dot{m}$	total mass flow rate of heat sink [kg/s]
N	number of measurement points
N_{ch}	number of micro-channels in heat sink
N_{pch}	dimensionless phase change parameter
N_{sub}	dimensionless subcooling parameter
p	pressure [Pa]
Pe	Peclet number
P_F	friction perimeter of channel [m]
P_H	heated perimeter of channel [m]
P_r	reduced pressure
Δp	pressure drop [Pa]
q''	heat flux [W/m^2]
q''_B	heat flux based on total base area of heat sink [W/m^2]
q''_H	heat flux based on heated perimeter of micro-channel [W/m^2]
Q	volumetric flow rate [m^3/s]
Q_g	vapor generation rate [m^3/s]
T	temperature [°C]
t	time; oscillation period [s]
T_{sat}	saturation temperature [°C]
T_w	wall temperature [°C]
$\bar{u}$	mean fluid velocity [m/s]
W_{ch}	width of micro-channel's cross-section [m]
We	Weber number

W_w	half-width of copper sidewall separating micro-channels [m]
x_e	thermodynamic equilibrium quality
x_k	sampling point in time, $0 \leq x_k \leq 2\pi$ [rad]
z	coordinate along micro-channel [m]

Greek symbols

α	thermal diffusivity [m^2/s]
δ	film thickness [μm]
η	fin efficiency
ρ	density [kg/m^3]
σ	surface tension [N/m]
τ	period [s]

Subscripts

avg	average
b	bottom of micro-channel
$evap$	evaporation
exp	experimental
f	liquid
fo	liquid-only
g	vapor
in	micro-channel inlet; inlet
out	micro-channel outlet; outlet
$pred$	predicted
s	solid material of heat sink
sat	saturation
sp	single-phase
$super$	superheated
tc	thermocouple
up	upstream plenum
w	wall

Acronyms

CHF	critical heat flux
DNB	departure from nucleate boiling
DWO	density-wave oscillation
EBO	explosive boiling oscillation
LED	Ledinegg instability
ONB	onset of nucleate boiling
PCI	parallel-channel instability
SPDO	severe pressure-drop oscillation

the channel diameter. However, the cooling performance of these single-phase devices is limited by their sole dependence on sensible heat rise of the coolant. On the other hand, two-phase heat sinks can achieve orders of magnitude enhancement in the heat transfer coefficient by utilizing the coolant's both sensible and latent heat. They also result in smaller temperature gradients both between the device and coolant, and axially along the channel.

Despite these merits, two-phase mini/micro-channel heat sinks are not without shortcomings. By decreasing the hydraulic diameter in order to increase the two-phase heat transfer coefficient, pressure drop across the channels can increase appreciably, resulting in significant compressibility (resulting from axial changes of vapor and liquid specific volumes with pressure) and flashing (resulting from axial changes of vapor and liquid enthalpies with pressure), as well as increased likelihood of two-phase choking [30]. These performance drawbacks are, in fact, closely related to the distinction between channel sizes: one to a few millimeters for mini-channels versus ten to several hundred micrometers for micro-channels. For example, Bowers and Mudawar [31] compared the cooling performances of a mini-channel heat sink with D_h = 2.5 mm to that of a micro-channel heat sink with D_h = 0.51 mm, and showed that, while they produce fairly similar heat transfer performances, the latter produced significantly higher pressure drop and incurred appreciable compressibility and flashing.

Recently, the authors of the present study explored the implementation of two-phase mini/micro-channel heat sinks as multi-kilowatt evaporators for future space vehicles that could tackle heat removal from both avionics and crew [32]. They also proposed the concept of using the same evaporators in a 'Hybrid Thermal Control System' (H-TCS) for space vehicles, allowing the cooling loop to be automatically reconfigured into a vapor compression loop, a pumped two-phase cooling loop, or a pumped single-phase loop.

1.3. Large length-to-diameter mini/micro-channels and heat sinks

Mini/micro-channels featuring large length-to-diameter ratios are especially instrumental for understanding the axial variations of flow patterns and heat transfer mechanisms. Many such studies have been focused on boiling in a single long channel, and revealed gradual changes in the dominant heat transfer mechanism, from nucleate flow boiling in the upstream low quality region to convective flow boiling in the downstream high quality region [33–36]. And high-speed video captured a succession of dominant flow patterns, namely bubbly, slug, churn, and annular [37,38]. But, from a practical point of view, two-phase mini/micro-channel heat sinks, which are comprised of a large number of channels extending between shared upstream and downstream plenums, are better suited for electronic cooling applications. The present authors have examined the two-phase transport characteristics of large length-to-diameter heat sinks [39]. They captured a series of dominant heat transfer mechanisms consisting of nucleate boiling, confined bubble boiling, convective boiling, and partial dryout. When used as evaporator in a vapor compression system [39], these heat sinks exhibited partial dry-out and complete dryout; both are closely associated with flow instabilities [40,41].

1.4. Instabilities in mini/micro-channel flow boiling

1.4.1. Static instability

As discussed in previous review articles [42,43], two-phase flow instabilities can be grouped into two main categories, *static* and *dynamic*. The system is deemed *statically stable* if, after disturbance, operating conditions are restored to pre-disturbance levels. Conversely, the system is deemed *statically unstable* if the new operating conditions are different from pre-disturbance levels. Operating conditions leading to *static instability* can be determined by comparing the flow loop's *internal characteristics curve* (pressure drop of flow boiling component versus mass velocity) and *external characteristics curve* (pressure drop of loop components excluding the flow boiling component versus mass velocity), and the condition for *Ledinegg (LED) instability*, the most well-known type of static instability, is expressed algebraically as [44]

$$\left(\frac{\partial \Delta p}{\partial G}\right)_{int} \leqslant \left(\frac{\partial \Delta p}{\partial G}\right)_{ext}. \tag{1}$$

As this inequality implies, occurrence of *LED* depends highly on the components and operating conditions dictating the external characteristics curve. However, Zhang et al. [45] demonstrated experimentally the susceptibility of a pumped loop incorporating a multi-channel heat sink to LED, and the increased likelihood of LED with increasing number of channels.

1.4.2. Dynamic instability

This form of instability is defined as flow oscillations sustained by feedback among flow rate, pressure drop, and density changes, depending on the rate of vapor generation in the boiling component.

Density-wave Oscillations (DWO) - This type of dynamic instability is observed mostly in micro-channel flow boiling [46,47], which, for a constant exit pressure, is manifest by a delayed response in mass flow rate to an increase in the pressure drop [48,49]. Because of small cross-section and high confinement effects, rapid bubble growth causes flow reversal and a corresponding increase in inlet plenum pressure [46], a primary cause of DWO in mini/micro-channels that is not evident in macro-channels. In fact, flow boiling experiments conducted by Saitoh et al. [47] using single tubes showed a drop in the heat transfer coefficient with decreasing hydraulic diameter, which they

attributed to DWO-induced dryout. They also showed that the amplitude of oscillations reaches peak value with inlet qualities close to $x_{e,in} = 0.13$, implying DWO and flow reversal are direct outcomes of increased vapor volume. Recently, O'Neill et al. [50] investigated the effects of DWO on system dynamics and assessed different stability criteria for flow boiling at different flow orientations [51].

Parallel-channel Instability (PCI) – This type of dynamic instability has been identified in parallel mini/micro-channels [52], and takes the form of relatively mild flow oscillations that persist even when severe pressure oscillations are eliminated by increasing upstream flow resistance with the aid of a throttling valve. This type of instability is manifest by random, albeit mild fluctuations in the inlet and outlet pressures. In fact, the amplitudes of pressure fluctuations in the plenums have been used to construct criteria for occurrence of PCI in parallel-channel heat sinks [46]. It is important to note that, while DWO can occur within individual channels, PCI is the result of pressure feedback among parallel channels sharing the same inlet and outlet plenums.

Severe Pressure-drop Oscillation (SPDO) - This is another type of dynamic instability that is associated with much longer oscillation periods ($\sim$10 min) [52–55] compared to those for DWO ($\sim$60 s) [56]. SPDO occurs in the negative slope region of the internal characteristics curve when the external characteristics curve has an algebraically smaller slope than the internal characteristics curve [44],

$$\left(\frac{\partial \Delta p}{\partial G}\right)_{int} > \left(\frac{\partial \Delta p}{\partial G}\right)_{ext}. \tag{2}$$

Maulbetsch and Griffith derived the above inequality for an unstable state using a lumped parameter model based on divergence in solution of the momentum equation [44,57–59]. SPDO associated with flow boiling in micro-channel heat sinks has received increased attention in recent years. Qu and Mudawar measured a SPDO amplitude of 0.3 bar and period of 10 s for a water heat sink containing 21 of 231–713-μm^2 rectangular micro-channels [52]. Zhang et al. [55] observed SPDO in water flow boiling in a micro-channel heat sink, and numerically solved the momentum equation using a nonlinear parameter identification technique.

1.5. Effects of flow oscillations on heat transfer characteristics of mini/micro-channel heat sinks

A few studies aimed to identify dominant parameters responsible for initiating flow oscillations in mini/micro-channel heat sinks, pointing to heat flux as the most crucial of these parameters [46,48,60]. These studies also report severe flow reversal resulting from rapid bubble growth caused by bubble confinement effects in small channels, which is followed by rapid nucleation once a heat flux threshold is exceeded. The frequency of oscillation has been reported to increase with increasing heat flux in the low heat flux range, but tends to fluctuate in the high flux range because of increasing interaction among the parallel channels [61–63].

A unique flow boiling oscillation phenomenon that has been observed at high heat fluxes and low Reynolds numbers is *Explosive Boiling Oscillation* (EBO) [64]. Qu and Mudawar [65] and Lee and Mudawar [14] observed this phenomenon in multi micro-channel heat sink flow boiling of water and HFE-7100, respectively, triggering critical heat flux (CHF) due to intense boiling and vapor backflow. EBO is associated with liquid surge and liquid deficient periods, and dryout occurs over the entire channel in the liquid deficient period. EBO frequency (6.67–50.0 Hz) is typically orders of magnitude greater than the oscillation frequency of the heat sink's plenum pressure (1.4–2.8 Hz) [62].

Oscillation frequency is also highly influenced by the heat sink's channel geometry. For example, heat sinks with increased flow area, such as those employing diverging channels [66] or cross-linked channels [67], increase the space available for bubble growth, thus reducing the intensity of oscillations. Studies have also shown a dependence of oscillation frequency on inlet plenum design [68], and vapor back flow on magnitude of oscillation [69]. Table 1 provides a summary of criteria for unstable flow boiling and the influence of channel configuration on oscillation amplitude.

Several studies have addressed the influence of periodic flow patterns, induced by vapor back flow [14,62,65] and flow oscillations [40,49,70,71], on the heat transfer coefficient and its degradation due to dryout [33,36,72,73] in micro-channel heat sinks. Recently, the authors of the present study observed intermittent dryout in the downstream region of a large L/D_h heat sink for low heat fluxes and low Reynolds numbers [39]. Oscillation frequency has been identified as one of the most important parameters for describing heat transfer in periodic flow boiling [70]. There have been a few attempts to develop predictive tools for oscillation frequency [62,67,74], however, no such tools have been developed for very large L/D_h heat sinks. It is imperative that large L/D_h heat sinks incur much higher confinement effects than those with small L/D_h. Table 2 provides a summary of studies concerning flow boiling instabilities in micro-channel heat sinks with different L/D_h ratios.

1.6. Objectives of study

Recent studies by the authors [39,40] involving large L/D_h multi-channel heat sinks have demonstrated close relationship between pressure oscillations and downstream intermittent dryout, and highlighted the importance of oscillation frequency to the dryout process. This study will address the parametric trends of oscillation frequency and identify key dimensionless parameters that govern frequency value. A new frequency correlation will be derived specifically for large L/D_h heat sinks. Also discussed will be detailed parametric trends of the local heat transfer coefficient, and determination of conditions leading to intermittent dryout in the downstream regions of the channels.

2. Experimental set-up

2.1. Two-phase flow loop

Shown in Fig. 1(a) is a schematic diagram of the two-phase cooling loop that is assembled for the purpose of delivering R134a to the micro-channel test module at desired operating conditions. R134a is selected for the study based on a number of considerations, including thermodynamic performance, maximum system pressure, flow rate requirements, and both safety and environmental concerns [32]. Fig. 1(b) shows a 3D CAD renderings of the entire test facility.

Heat is supplied to the micro-channel module from a thick-film heater situated beneath the test module's copper heat sink (described below). The fluid enters the micro-channel module is subcooled state and gradually changes phase from liquid to vapor along the micro-channels. The two-phase mixture exiting the test module is routed to an air-cooled condenser, where it is returned to liquid state by rejecting heat to the ambient. The amount of sub-cooling at the condenser's exit is determined by the condenser's fan speed, which is regulated by a solid-state controller. Constant pressure is maintained in the loop's liquid reservoir by simultaneously heating the reservoir's liquid with the aid of a PID-controlled electric heater, and condensing the reservoir's vapor using a helical condenser that is cooled by a Lytron modular cooling system. The liquid is subcooled further by flowing through a SWEP plate-type heat exchanger that is cooled by a second modular cooling system, ensuring that no vapor enters the downstream Micro-pump GB series gear pump or turbine flow meter. The flow cycle is completed as the fluid is returned to the micro-channel module.

2.2. Construction and instrumentation of the micro-channel module

Fig. 2(a) shows 3D CAD renderings of the layered construction of the micro-channel test module. Multiple layers are shown embracing the pure copper heat sink, the central component of the test module. The copper heat sink has a top heat transfer area measuring 609.6-mm long by 203.2-mm wide, machined into which are 100 of 1×1 mm^2 micro-channels. Uniform heat flux is supplied from a Watlow thick-film heater situated beneath the heat sink. The heat sink temperatures are measured along the centerline by type-E thermocouples inserted at several axial locations as indicated in Table 3. The heat sink and thick film heater are contained in an insulating housing made from G-7 fiberglass and insulated beneath by a layer of G-10 fiberglass. The tops of the micro-channels are closed off by a transparent cover plate made from polycarbonate plastic, which also provides optical access to the two-phase flow along the micro-channels. The entire test module assembly is pressed tightly together with the aid of a stainless steel cover brace and aluminum support bars atop, and aluminum support bars below. This support is intended to preclude buckling of the intermediate layers, as well as close off any gaps between the top surface of the heat sink and the cover plate. The inlet and outlet plenums of the test module possess four flow ports each, which serve to ensure uniformity of flow distribution among the micro-channels.

Table 1
Unstable flow boiling oscillation criteria.

Author(s)	Criteria	Remarks
Saha et al. [48]	$N_{sub} = 0.0022 Pe \frac{A}{P_H L_H} N_{pch}$ for $Pe \leqslant 70,000$	Thermal equilibrium model
	$N_{sub} = 154 \, Pe \frac{A}{P_H L_H} N_{pch}$ for $Pe \geqslant 70,000$	Single macro-channel
	$Pe = (\rho_f \, \bar{u}_{f,in} D_h \, c_{p,f})/k_f$	D_h = 10 mm
		L_H = 2.743 m
		R-113
Brutin et al. [60]	p_{in} or p_{out} > 1 kPa	Single rectangular micro-channel
	or $p_{peak}^2/p_{avg,noise}^2$ > 20	4×0.5 mm^2
		n-Pantane
Chang and Pan [46]	$\delta(\Delta p) \geq 6$ kPa	Multi rectangular micro-channel heat sink
		99.4 $\times$ 76.3 μm^2
		Water
Lu and Pan [66]	$\delta(\Delta p) \geq 3$ kPa	Multi rectangular micro-channel heat sink with 0.5° a diverging cross-section
		99.4 $\times$ 76.3 μm^2
		Water

Table 2
Previous studies on flow boiling instabilities in micro-channel heat sinks.

| Author(s)	Instability type[*]	Operating conditions	Channel geometry	Remarks[*,**,***]
Brutin et al. [60]	DWO	G = 125–475 kg/m^2 q_H'' = 200–700 kW/m^2	L = 50, 200 mm $W_{ch} \times H_{ch}$ = 4 $\times$ 0.5 mm^2 D_h = 0.889 mm L/D_h =56.2, 225.0	R S n-Pentane
Hetsroni et al. [73]	PCI	G = 69.0–276.0, 86.4–363.0, 44.2–232.2 kg/m^2 q_H'' = 80–300, 90–360, 51–500 kW/m^2	L = 15 mm D_h = 0.129, 0.103, 0.161 mm L/D_h = 116.3, 145.6, 93.2	T M Water
Brutin and Tadrist [75]	DWO	G = 95.8–2258 kg/m^2 q_H'' = 15.7–125.6 kW/m^2	L = 50, 200 mm $W_{ch} \times H_{ch}$ = 4 $\times$ 0.5 mm^2 D_h = 0.889 mm L/D_h = 56.2, 225.0	C S n-Pentane
Qu and Mudawar [65]	EBO, PCI	G = 85.9–368.4 kg/m^2 q_B'' = 0–2078.5 kW/m^2	L = 44.8 mm $W_{ch} \times H_{ch}$ = 0.231 $\times$ 0.712 mm^2 D_h = 0.349 mm L/D_h = 128.4	R M water
Qu and Mudawar [52]	PCI, SPDO	G=134.9–400.1 kg/m^2 q_B'' = 0–2400 kW/m^2	L = 44.8 mm $W_{ch} \times H_{ch}$ = 0.231 $\times$ 0.712 mm^2 D_h = 0.349 mm L/D_h = 128.4	R M Water
Wu and Cheng [76]	PCI, SPDO	G = 112–146 kg/m^2 q_H'' = 135.0–226.0 kW/m^2	L = 30 mm D_h = 0.186 mm L/D_h = 161.3	TZ M Water
Balasubramanian and Kandlikar [61]	PCI	G = 112–120 kg/m^2 q_H'' = 208–316 226.0 kW/m^2	L = 63.5 mm $W_{ch} \times H_{ch}$ = 0.990 $\times$ 0.207 mm^2 D_h = 0.333 mm L/D_h = 190.7	R M Water
Hetsroni et al. [64]	EBO, PCI	G = 95–340 kg/m^2 q_H'' = 80–330 226.0 kW/m^2	L = 15 mm D_h=0.129 mm L/D_h=116.3	T M Water
Xu et al. [77]	PCI, SPDO	G = 20–1200 kg/m^2 q_H'' = 35.7–160.4 kW/m^2	L = 50 mm $W_{ch} \times H_{ch}$ = 0.3 $\times$ 0.8 mm^2 D_h = 0.436 mm L/D_h = 114.7	R M Water Methanol
Hetsroni et al. [62]	EBO, PCI	G = 32.0–200 kg/m^2 q_H'' = 120.0–270.0 kW/m^2	L = 15 mm D_h = 0.1, 0.13, 0.22 mm L/D_h = 150, 115.4, 227.3	T M Water, ethanol
Chang and Pan [46]	PCI	G = 22–110 kg/m^2 q_H'' = 7.86–95.5 kW/m^2	L = 14 mm $W_{ch} \times H_{ch}$ = 0.0994 $\times$ 0.0763 mm^2 D_h = 0.0863 mm L/D_h = 162.2	R M water
Muwanga et al. [67]	PCI	G = 91–228 kg/m^2 q_H'' = 0–100 kW/m^2	L = 16 mm $W_{ch} \times H_{ch}$ = 0.269 $\times$ 0.283 mm^2 D_h = 0.2758 mm L/D_h = 58	R M water
Wang et al. [78]	PCI	G = 142.3–311.2 (M) 950–3523.2 (S) kg/m^2 q_H'' = 226.9–497.8 (M), 84.5–297.8 (S) kW/m^2	L = 30 mm D_h = 0.186 mm L/D_h = 161.3	TZ S, M Water
Lu and Pan [66]	PCI	G = 99–297 kg/m^2 q_H'' = 10–400 kW/m^2	L = 26 mm $W_{ch} \times H_{ch}$ = (inlet: 0.1–outlet: 0.56) $\times$ 0.076 mm^2 D_h = 0.12 mm L/D_h = 217	R M Water Diverging cross-section (0.5° angle)
Wang et al. [68]	PCI	G = 91.4–787.3 kg/m^2 q_H'' = 184.2–485.5 kW/m^2	L = 30 mm D_h = 0.186 mm L/D_h = 161.3	TR M Water Type-B
Bogojevic et al. [79,80]	PCI	G = 72.2–433.3 kg/m^2 q_H'' = 178–445 kW/m^2	L = 15 mm $W_{ch} \times H_{ch}$=0.15 $\times$ 0.273 mm^2 D_h = 0.194 mm L/D_h = 77.3	R M water
Zhang et al. [45]	LED	G = 0–1200 kg/m^2 q_H'' = 9.7–19.3, 16.1–32.3, 17.2–34.3 kW/m^2	L = 15 mm $W_{ch} \times H_{ch}$ = 0.061 $\times$ 0.272, 0.165 $\times$ 0.330, 0.340 $\times$ 0.335 mm^2 D_h = 0.1, 0.22, 0.337 mm L/D_h = 150, 68.2, 44.5	R M Water, HFE-7100
Zhang et al. [55]	SPDO	G = 0–1200 kg/m^2 q_H'' = 9.7–19.3 kW/m^2	L = 15 mm $W_{ch} \times H_{ch}$ = 0.061 $\times$ 0.272 mm^2 D_h = 0.1 mm L/D_h = 150	R M Water

Table 2 (continued)

Author(s)	Instability type[°]	Operating conditions	Channel geometry	Remarks[*,**]
Lee and Mudawar [40]	PCI	G = 75.9–436.6 kg/m^2 q_H'' = 2.7–29.6 kW/m^2	L = 609.6 mm $W_{ch} \times H_{ch}$ = 1.0 × 1.0^2 D_h = 1.0 mm L/D_h = 609.6	R M R134a

[°] DWO: density-wave oscillations, EBO: explosive boiling oscillations, PCI: parallel-channel instability, SPDO: severe pressure-drop oscillations, LED: Ledinegg instability.
[*] R: rectangular, C: circular, T: triangular, TZ: trapezoidal.
[**] S: single-channel, M: multi-channel.
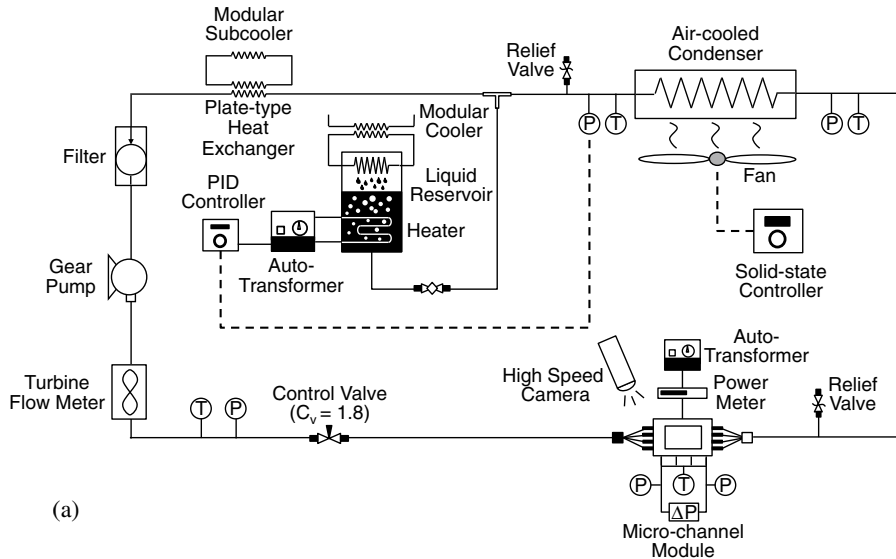
(a)
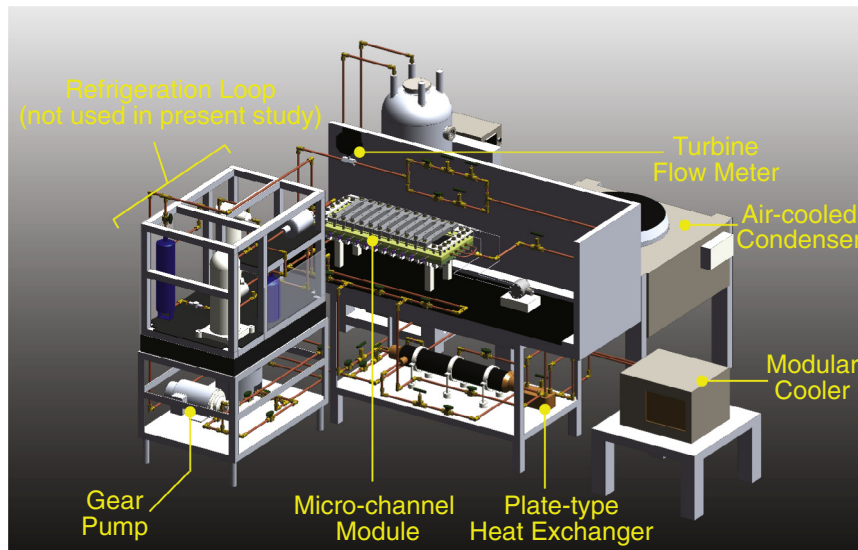
(b)

Fig. 1. (a) Schematic diagram of two-phase loop. (b) 3D CAD rendering of test facility.

Power input to the heat sink is measured by a Yokogawa WT310 power meter. Pressure drop across the micro-channels is measured by a combination of two Omega-MMA absolute pressure transducers connected to the inlet and outlet plenums, and a Honeywell-THE differential pressure transducer connected between the two plenums. The type-E thermocouples are chosen for their highest measurement sensitivity, 68 μV/°C, among the different high temperature thermocouple types. The volumetric flow rate is measured by a Flow Technology FTO series turbine flow meter. An FET multiplexer collects signals from the thermocouples, pressure

(a)

(b)

(c)
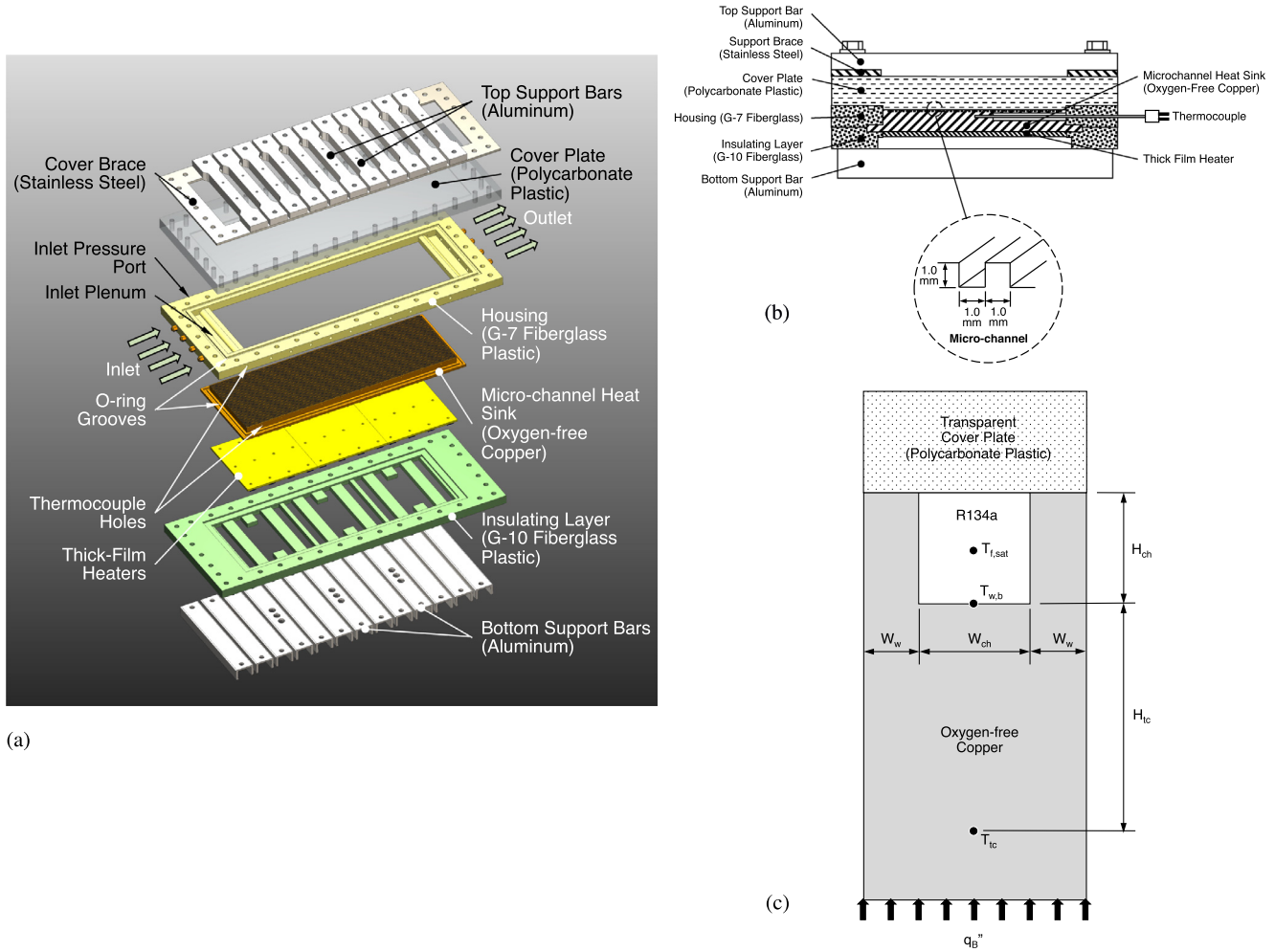
Fig. 2. Micro-channel module design: (a) CAD rendering, (b) cross-sectional view, and (c) two-dimensional micro-channel unit cell.

Table 3
Dimensions of the copper micro-channel heat sink and axial locations of the heat sink thermocouples.

Length [mm]	Width [mm]	Number of Channels	Thermocouple Axial Locations [mm]
609.6	203.2	100	44.2, 102.1, 160.0, 217.9, 275.8, 333.8, 391.7, 434.3, 507.5, 565.4

Table 4
Measurement error and uncertainty propagation.

Parameter	Error	Parameter	Uncertainty
Absolute pressure	±0.1%	Heat transfer coefficient, h	≤5.92%
Differential pressure	±0.1%	Pressure drop, Δp	≤0.1%
Temperature, T	±0.5%	Vapor quality change, Δx_e	≤3.23%
Mass flow rate, $\dot{m}$	±0.12%		
Heat input, Q	±0.3%		

transducers, flow meter, and power meter, which are processed by an HP data acquisition system. Measurement errors and uncertainty propagated in key calculated parameters (using root sum square method) are provided in Table 4.

Images of the two-phase flow along the micro-channels are captured with the aid of a Photron-Ultima APX high-speed camera fitted with a 105-mm Nikkor lens. This camera is capable of shutter speeds as high as 1/120,000 s.

2.3. Operating conditions

The micro-channel module's inlet quality, $x_{e,in}$, is determined from the relation

$$x_{e,in} = \frac{h_{in} - h_f}{h_{fg}} = -\frac{c_{p,f}(T_{sat} - T_{in})}{h_{fg}}, \tag{3}$$

where $c_{p,f}$, T_{sat}, and h_{fg} are based on saturation pressure measured at the module's inlet, and T_{in} is the measured inlet temperature. The

outlet quality is determined by applying an energy balance to the entire module,

$$x_{e,out} = x_{e,in} + (q_B'' A_{base})/\dot{m} h_{fg}, \tag{4}$$

where q_B'' is the heat flux based on the 609.6-mm long by 203.2-mm wide base area, A_{base}, of the heat sink, and $\dot{m}$ the total mass flow rate of R134a. Table 5 provides the detailed operating conditions tested in the study.

2.4. Determination of heat transfer coefficient

Shown in Fig. 2(b) is a cross-sectional diagram of the micro-channel test module assembly. The thermocouples are inserted transversely up to the heat sink's centerline where the thermocouple junctions are embedded. Fig. 2(c) shows a unit cell consisting of a single micro-channel and half the thicknesses of copper walls on

Table 5
Operating conditions of micro-channel module.

G [kg/m^{2}s]	q_B'' [W/m^2]	$x_{e,in}$	$x_{e,out}$	p_{in} [kPa]	Number of Δp data points (69 total)
75.92	4005–10,094	−0.031 to −0.022	0.331–0.893	688.3–690.0	4
94.90	3990–12,185	−0.032 to −0.026	0.256–0.853	690.7–691.6	5
113.88	4039–16,184	−0.039 to −0.025	0.206–0.956	691.5–695.0	7
132.86	4074–17,999	−0.038 to −0.026	0.174–0.908	692.7–699.2	8
151.85	4003–20,185	−0.038 to −0.029	0.148–0.892	693.1–704.3	9
170.83	3993–24,028	−0.040 to −0.031	0.128–0.944	694.1–711.9	11
189.81	4031–26,209	−0.040 to −0.030	0.111–0.928	695.0–721.4	12
208.79	4039–28,209	−0.041 to −0.030	0.096–0.927	695.9–731.3	13

Table 6
Dimensions of micro-channel heat sink unit cell.

W_w [mm]	W_{ch} [mm]	H_{ch} [mm]	H_{tc} [mm]
0.5	1.0	1.0	4.08

either side. Detailed dimensions of the unit cell are provided in Table 6. The two-phase heat transfer coefficient is determined by equating heat input from the underside of the copper heat sink to convection along the micro-channel walls, with the sidewalls treated as fins,

$$h_{tp} = \frac{q_B''(W_{ch} + 2W_w)}{(T_{w,b} - T_{f,sat})(W_{ch} + 2\eta H_{ch})}. \qquad (5)$$

The fin efficiency, η, is based on the assumption of adiabatic tip, $\eta = \tanh(mH_{ch})/(mH_{ch})$, where m the fin parameter given by $m = \sqrt{h/(k_s W_w)}$ [81].

The micro-channel's bottom wall temperature, $T_{w,b}$, is calculated by assuming one-dimensional heat conduction between the planes of the thermocouple and micro-channel's bottom wall,

$$T_{w,b} = T_{tc} - q_B'' H_{tc}/k_s, \qquad (6)$$

where H_{tc} and k_s are the distance between the thermocouple junction and micro-channel's bottom wall, and thermal conductivity of copper, respectively. The fluid saturation temperature, $T_{f,sat}$, in the micro-channels is determined from the corresponding saturation pressure, which is calculated by linear interpolation between the inlet and outlet pressures.

3. Experimental and statistical results of pressure oscillations

3.1. High-speed images of vapor backflow in inlet plenum

Fig. 3(a) shows images of periodic vapor back flow in the heat sinks' inlet plenum for G = 170.83 kg/m^{2}s and four heat fluxes in the range of q_B'' = 18,164–24,219 W/m^2. Two representative images are shown for each heat flux, one captured at the beginning of the backflow period, and a second the middle of the period. Notice that, because of increased rate of vapor generation, the period decreases with increasing heat flux, 1424, 1304, 1200 and 1096 ms for heat fluxes of 18,164, 20,182, 22,201 and 24,219 W/m^2, respectively. Here, the backflow period is defined as the time that the sinusoidal shaped bubble mass in the upstream plenum completes one cycle. Fig. 3(b) shows, for G = 170.83 kg/m^{2}s and q_B'' = 24,219 W/m^2, a sequence of flow images of the inlet plenum encompassing a full period of the backflow. Physically, the vapor backflow period may be described as follows. Initially, intense vapor generation increases flow resistance along the channel, causing the vapor to follow backwards to the inlet plenum, which also increases the inlet plenum pressure. The now high inlet

plenum pressure begins to push the flow downstream through the micro-channels. This, in turn, serves to decrease the inlet plenum pressure, followed by a new phase of intense vapor generation. Notice in Fig. 3(b) that the vapor backflow does not occur simultaneously in all the channels, but is preferential to channels along one side of the plenum.

While flow maldistribution in the lateral direction is a common occurrence with micro-channel heat sinks, this problem was minimized in the present study by employing a flow distributor upstream of the micro-channel module. The periodic behavior described in conjunction with Fig. 3 is different from that commonly encountered in multi-channel heat sinks. In the present study, flow periodicity along the axial direction is far more significant than the lateral direction. This is confirmed experimentally by the observation that the period captured along the centerline using high speed video closely matching the period of backflow oscillation in the inlet. The axial periodicity is also reflected in the temperature measurements at the centerline. Furthermore, the present findings point to periodic dryout that is more dominant along the axial direction than the lateral.

3.2. Frequency and power density spectrum analysis of pressure oscillation data

Fig. 4(a) shows 50-s temporal records of the test module's pressure drop oscillations for G = 170.83 kg/m^{2}s and four heat fluxes in the range of q_B'' = 16,083–24,219 W/m^2. The most obvious observations from this figure are (a) increased amplitude of pressure drop oscillations and (b) increased frequency of oscillations with increasing heat flux. To preserve consistency in analyzing temporal records, all pressure drop signals are truncated at N = 2321, the total number of measurement points, to have equal number of sampling points for a discrete Fourier transform over the same time domain of 614.3 s. Additionally, the signals are converted to frequency domain at a sampling frequency of 3.78 Hz. The Fourier transform of pressure drop time record, f_k, is expressed in complex form of Fourier series as [82]

$$f_k = f(x_k) = \sum_{n=0}^{N-1} C_n e^{-inx_k} \quad n = 0, 1, \ldots, N-1, \qquad (7)$$

where x_k represents the sampling points in time, $x_k = 2\pi k/N$, N the total number of measurement points, and C_n the complex Fourier coefficient of f_k at sampling frequency nx_k.

$$C_n = \frac{1}{N}\sum_{k=0}^{N-1} f_k e^{-inx_k}. \qquad (8)$$

The discrete Fourier transform is expressed as

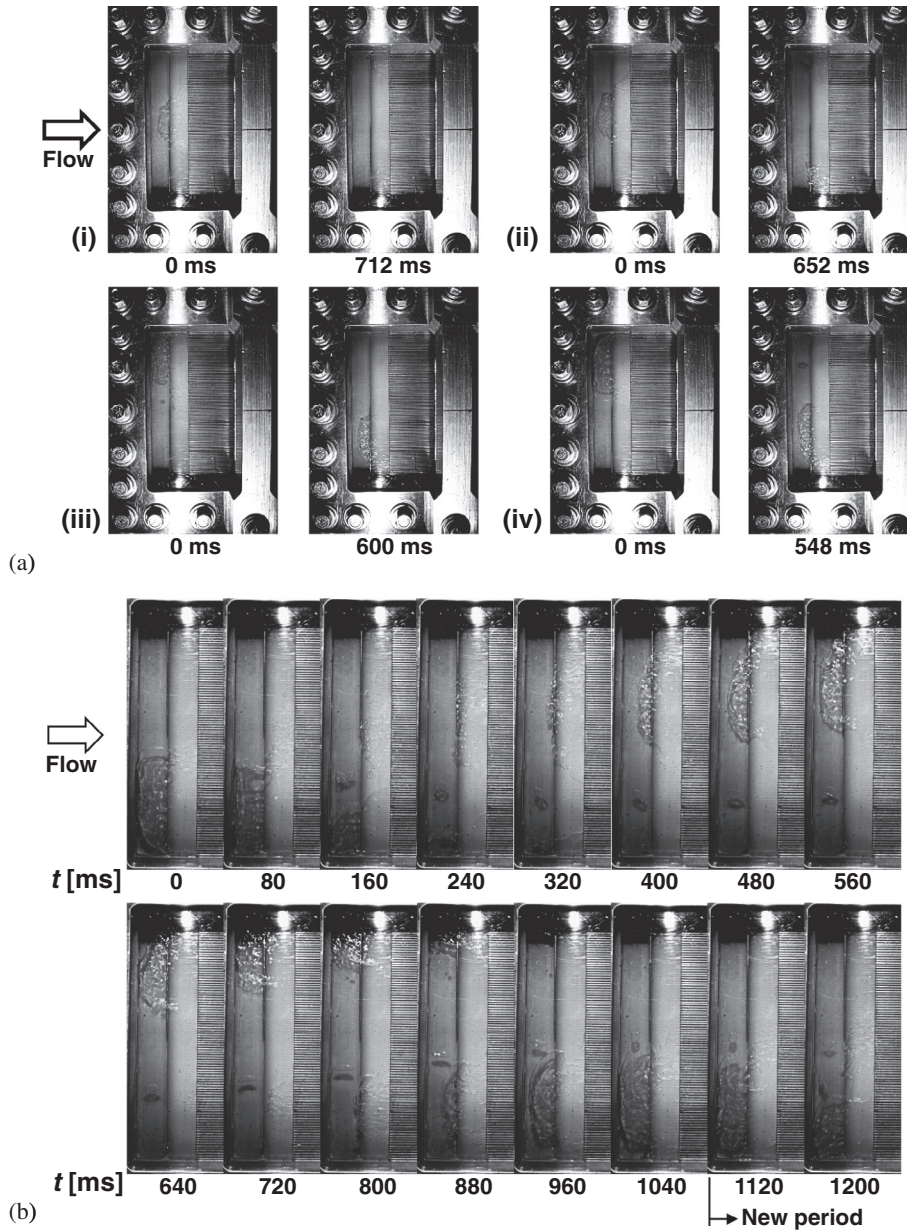$$\hat{f}_n = NC_n = \sum_{k=0}^{N-1} f_k e^{-inx_k}, \qquad (9)$$

Fig. 3. Images of vapor backflow in inlet plenum. (a) Two representative images in a half period for G = 170.83 kg/m^2 s with heat flux, q_B'' and corresponding period of (i) 18,164 W/m^2 and 1424 ms, (ii) 20,182 W/m^2 and 1304 ms, (iii) 22,201 W/m^2 and 1200 ms, and (iv) 24,219 W/m^2 and 1096 ms, respectively. (b) Sequence of flow oscillation images for G = 170.83 kg/m^2 s and q_B'' = 24,219 W/m^2.

and, using Matlab [83], and the average power density spectrum is determined as

$$\overline{P} = \frac{1}{N}\sum_{n=0}^{N-1}\hat{f}_n\hat{f}_n^*, \tag{10}$$

where $\hat{f}_n^*$ is the complex conjugate of Fourier transform. Fig. 4(b) shows the average power spectrum of pressure drop records. Both amplitude and frequency show significant and monotonic increases with increasing heat flux. The oscillation frequencies identified using the discrete Fourier transform are 0.706, 0.764, 0.830, and 0.913 Hz for heat fluxes of 18,164, 20,182, 22,201, and 24,219 W/ m^2, respectively. These frequencies are close to the measured frequencies of 0.702, 0.767, 0.833, and 0.912 Hz, associated with the vapor backflow, Fig. 3(a), and determined from reciprocals of the time periods, 1/1424, 1/1304, 1/1200, and 1/1096 ms^{-1}, respectively.

3.3. Impact of pressure oscillations on heat transfer performance of heat sink

Pressure oscillations induced by the vapor backflow can have a profound influence on the local heat transfer coefficient along the channel. This is especially a concern in the downstream regions of the channels incurring quality values approaching unity. Here, fluctuations associated with the vapor backflow can lead to intermittent downstream dryout if the annular liquid film is locally evaporated before the next liquid surge of the instability period. This phenomenon is captured in Fig. 5(a) for conditions associated with high quality values, evidenced by a sharp decline in the local heat transfer coefficient due to intermittent dryout, especially for the highest heat flux. q_B'' = 24,219 W/m^2. Another manifestation of the same phenomenon is a substantial increase in the fluid superheat measured in the test module's outlet plenum, $T_{super,out} - T_{sat,out}$, for $q_B'' \geq 22,201$ W/m^2, Fig. 5(b), even where x_e
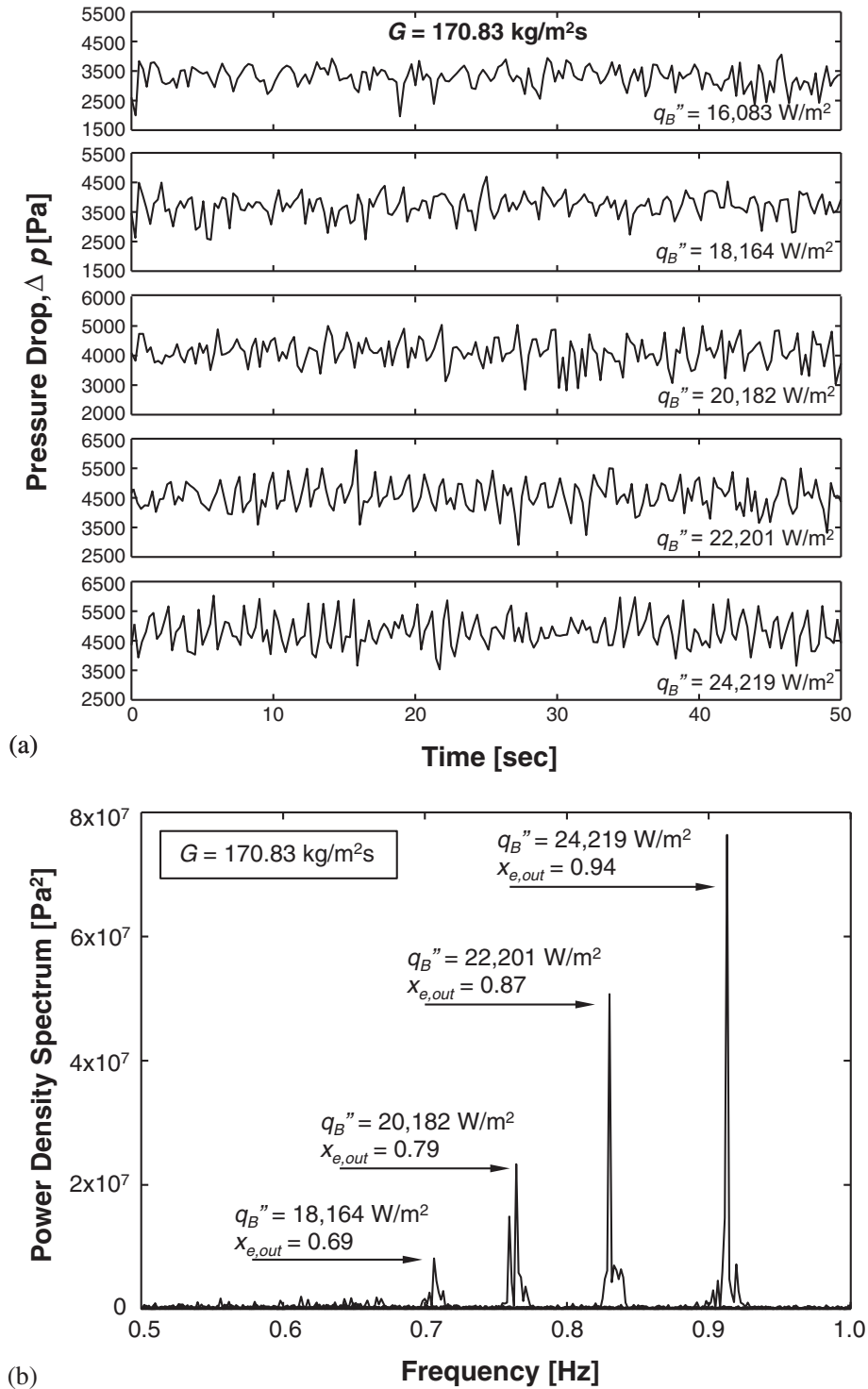
Fig. 4. Assessment of heat flux effects on flow oscillations for G = 170.83 kg/m² s: (a) pressure drop oscillation in time domain, and (b) corresponding power density spectrum by fast Fourier transform (FFT) in frequency domain.

is below unity. This is also captured in Fig. 5(c), where the outlet superheat is shown suddenly increasing above $x_{e,out}$ = 0.8. The influence of the vapor backflow is also felt in the inlet plenum, which is manifest by the temperature measured in the inlet plenum, T_{in}, exceeding the liquid temperature, T_{up}, measured upstream of the test module. Fig. 5(d) shows the difference between the two temperatures, $\Delta T_{up,in} = T_{in} - T_{up}$, which increases as the vapor backflow is intensified with increasing heat flux. For mass velocities in the range of G = 132.86–170.83 kg/m² s, this

temperature difference increases with increasing heat flux, reaching peak value before decreasing with a further increase in the heat flux.

The inlet temperature increase depicted in Fig. 5(d) has been reported in a previous study [66] both with or without vapor backflow to the inlet plenum, which indicates this temperature increase can result from both single-phase and two-phase mixing. It is important to note that, while both intermittent dryout and premature CHF [14] are associated with flow oscillations and vapor
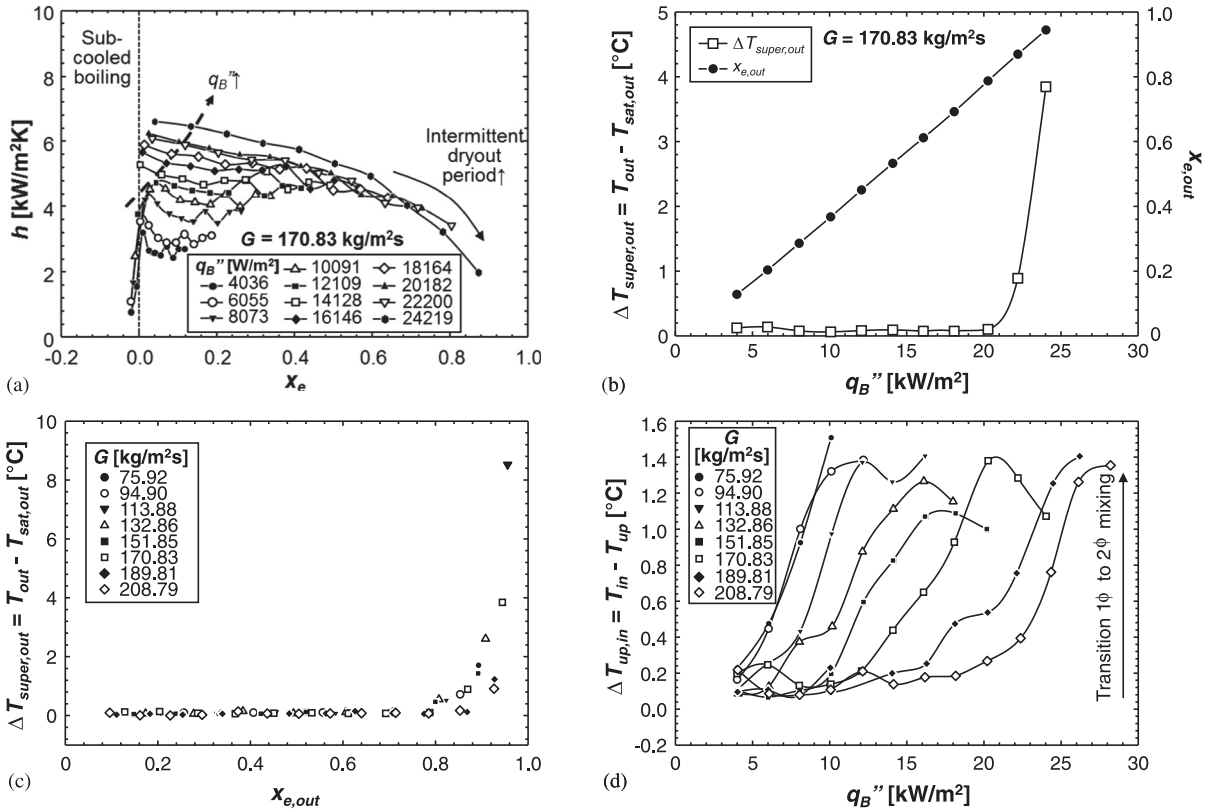
Fig. 5. Temperature changes in the inlet and outlet plenums for different operating conditions; data are time-averaged over 5 min after reaching steady state. (a) Variations of local heat transfer coefficient with quality for G = 170.83 kg/m^2 s and different heat fluxes. (b) Variations of outlet plenum superheat and quality with heat flux for G = 170.83 kg/m^2 s. (c) Variations of outlet plenum superheat with exit quality for different mass velocities. (d) Variations of measured inlet temperature relative to liquid temperature upstream of test module with increasing heat flux for different mass velocities.

backflow, they are fundamentally different in that intermittent dryout is encountered in saturated flow boiling at low heat fluxes and low mass velocities, conditions associated with high exit quality, while premature-CHF is encountered at high heat fluxes and high mass velocities, and occurs even with negative exit quality.

3.4. Effects of heat flux and mass velocity on pressure oscillations

Fig. 6(a)–(d) provide an assessment of the influences of heat flux and mass velocity on pressure oscillations using the discrete Fourier transform (DFT). Fig. 6(a) shows the power density spectrum of pressure oscillation amplitude versus heat flux for different mass velocities. It shows an abrupt increase in the power density spectrum corresponding to the onset of parallel-channel instability (PCI) for each mass velocity once a threshold heat flux is exceeded, and the heat flux threshold increases with increasing mass velocity. Fig. 6(b) shows a much clearer and fairly linear dependence of oscillation frequency on heat flux. Interestingly, Fig. 6(b) also points to a lack of dependence of oscillation frequency on mass velocity, which is consistent with observations from previous studies [46,48]. Oscillation frequency is also governed by liquid inertia from the inlet to the flow reversal point, as well as the stiffness of compressible volume in the inlet plenum, resembling resonance in a mechanically vibrating system. Notice that the effects of liquid inertia on amplitude and frequency are clearly captured in the present study, given the large length to diameter ratio of L/D_h = 609.6 used. Bruin et al. [60] presented resonance characteristics versus heat flux and mass velocity resembling those in Fig. 6(a) and (c), and indicated that vapor

blackflow increases the inlet plenum's compressible volume. Fig. 6(c) shows the amplitude increases with increasing mass velocity up to peak value then decreases as high liquid inertia begins to suppress oscillations, and the mass velocity corresponding to peak amplitude increases with increasing heat flux. Fig. 6(d) shows mass velocity has a relatively weak influence on oscillation frequency.

4. New correlation for oscillation frequency

4.1. Comparison with prior relations for oscillation frequency

Table 7 provides a list of prior relations for pressure oscillation frequency for single-channel and multi-channel flow boiling, along with their accuracy in predicting frequencies measured in the present study and determined by Fourier transform. Fig. 7(a)–(c) show detailed comparisons with predictions of Plesset and Zwick [84], Jacobi and Thome [74], and Hetsroni et al. [62], respectively. Dupont et al. [74] suggested the onset of nucleate boiling (ONB) occurs at x_e = 0 and that the frequency of periodic flow is dictated by the time it takes a bubble to grow to the channel diameter. They derived a correlation for frequency based on a three-zone periodic flow model [70], which does not explain the flow oscillation physics despite good predictions of their data. Their frequency was based on Plesset and Zwick's model for bubble growth in superheated liquids. Fig. 7(a) shows the Plesset and Zwick model underpredicts the present frequency data with a MAE of 60.4%. Physically, bubble growth alone cannot explain the DWO induced by rapid pressure drop. Additionally, there are appreciable differences in oscillations occurring in a single-channel compared
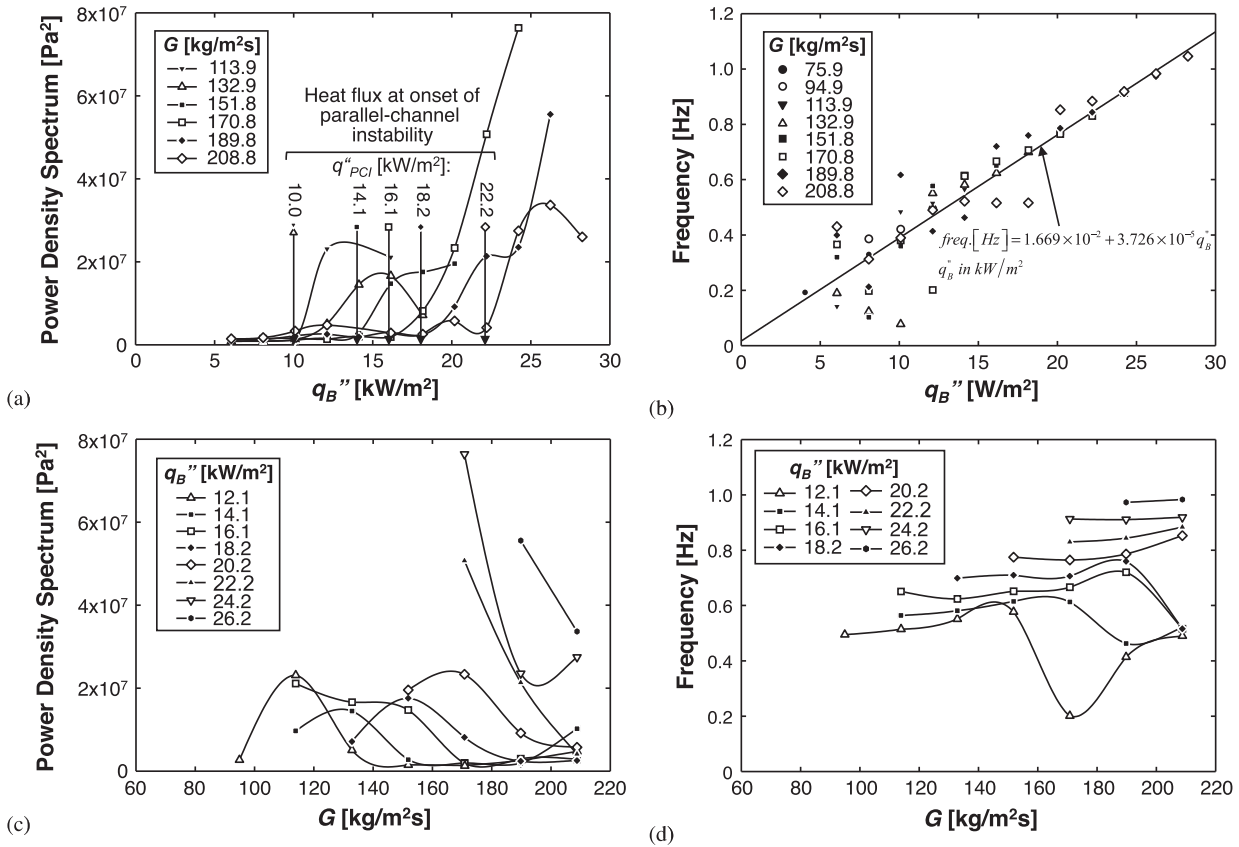
Fig. 6. Assessment of effects of operating conditions on flow oscillations using discrete Fourier transform (DFT): (a) Power density spectrum of pressure oscillation amplitude versus heat flux. (b) Oscillation frequency versus heat flux. (c) Power density spectrum of pressure oscillation amplitude versus mass velocity. (d) Oscillation frequency versus mass velocity.

Table 7
Previous relations for flow boiling oscillation frequency.

Author(s)	Relations	Remarks
Plesset and Zwick [84]	$f = 1/\tau = \left[\frac{2\rho_f c_{pf} \Delta T_{sat,avg}}{\rho_g \Delta h_{fg} D_h}\right]^2 \frac{12\alpha_f}{\pi}$ $\Delta T_{sat,avg} = T_{w,avg} - T_{sat,avg}, \alpha_f = \frac{k_f}{\rho_f c_{pf}}$	Analytical model for bubble growth rate in superheated liquid MAE=60.4%
Dupont et al. [74]	$f = (q_H''/q_{ref}'')^{1.74}$ $q_{ref}'' = 3328(P_r)^{-0.5}$	Single circular tube; multi-channel with circular and rectangular channels CO_2, R11, R113, R12, R123, R-134a/, R141 b MAE=170.9%
Hetsroni et al. [62]	$f = [0.000030 \ \bar{u}D_h Bo^{-2}]^{-1}$ $\bar{u} \simeq j_f, Bo = q_H''/(Gh_{fg})$	Frequency for explosive boiling oscillation (EBO) in single micro-channel Water, ethanol MAE=6619.8%
Muwanga et al. [67]	$f = \frac{\bar{u}_{in}}{L} C_1 Bo^{C_2} N_{sub}^{C_3} We^{C_4} N_{ch}^{C_5}$ $C_1 = 3.383 \times 10^{-15}, C_2 = -1.408, C_3 = 4.328,$ $C_4 = 0.144, C_5 = -0.137$ $We = (G^2 D_h/\sigma\rho_f), \bar{u}_{in} = j_{f,in}$	Frequency for explosive boiling oscillation (EBO) in multi micro-channel heat sink Distilled water MAE=99.9%

to those in a multi-channel heat sink. Fig. 7(b) shows the frequency relation by Jacobi and Thome overpredicts the present frequency data with a MAE of 170.9%. Hetsroni et al. reported that the temporal dryout associated with explosive boiling oscillation (EBO), which occurs at relatively high heat fluxes ($q_H'' = 120$–270 kW/m²) and low mass velocities ($G = 32$–200 kg/m² s), leads to significant out-of-phase high frequency oscillations in individual channels of a multi-channel heat sink, and increases waiting time for re-wetting. Fig. 7(c) shows

appreciable departure of the EBO frequency predictions from the present data, evidenced by a MAE of 6619.8%. Another frequency correlation by Muwanga [67], developed for multi-channel heat sink, underpredicts the present data with a MAE of 99.9%, which may be explained by their use of a length-to-diameter ratio, L/D_h, that is smaller than those of most other studies as indicated in Table 2. Failure of the available frequency relations to predict the present data points to the need for a new and improved frequency correlation.
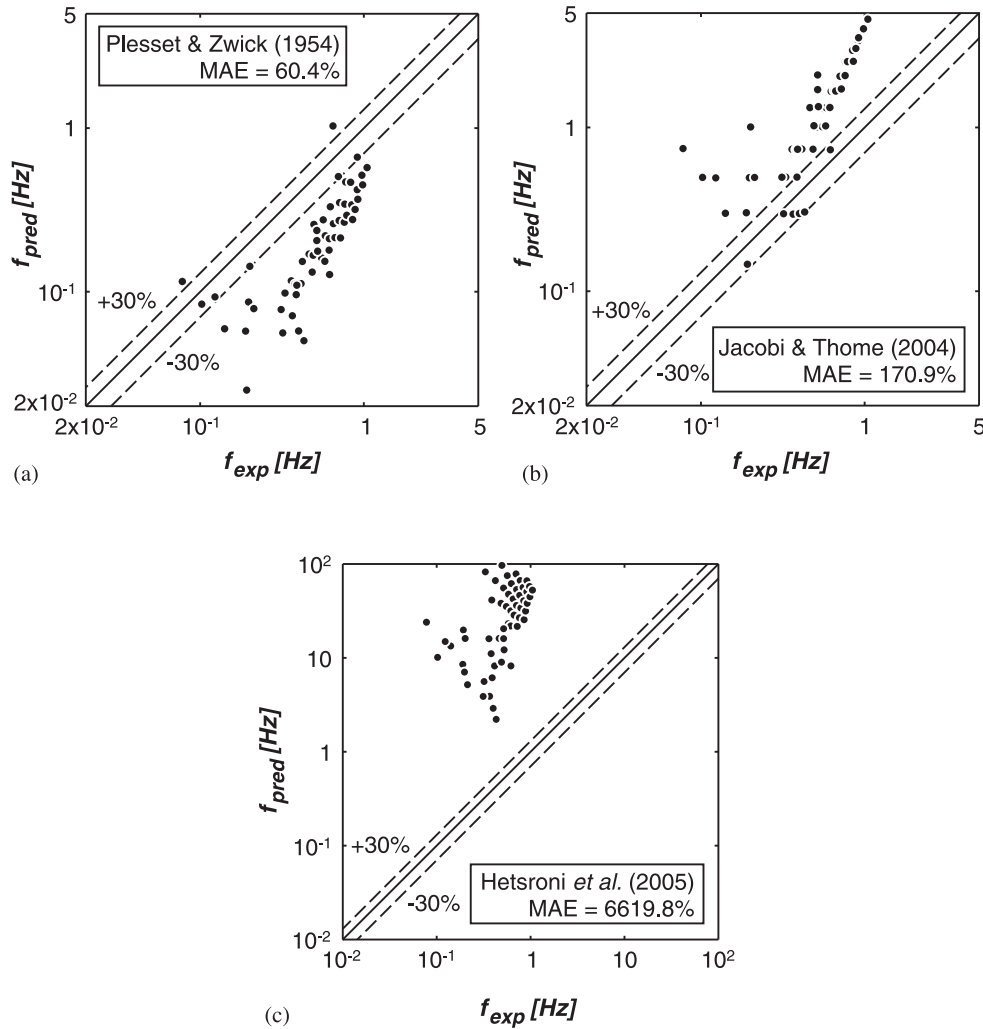
Fig. 7. Assessment of previous frequency relations against present pressure drop oscillation data: (a) Plesset and Zwick [84], (b) Jacobi and Thome [74], and (c) Hetsroni et al. [62].

4.2. Determination of dominant non-dimensional parameters

As discussed earlier in regards to the influences of heat flux and mass velocity, the amplitude and frequency of the complex oscillation phenomena observed in the present study are closely associated with vapor generation rate, as suggested in a previous study by Brutin et al. [60]. To determine dominant non-dimensional parameters governing the pressure oscillations, three parameters that influence vapor generation are examined: (a) rate of total vapor generation, ΔQ_g, (b) rate of vapor generation per unit length, dQ_g/dz, and (c) extent of upstream single-phase liquid length, $L_{sp,f}$, from the inlet to the location where $x_e = 0$, which are expressed, respectively, as

$$\Delta Q_g = \frac{q_B''(W_{ch} + 2W_w)N_{ch}(L - L_{sp,f})}{\rho_{g,in}h_{fg,in}}, \tag{11}$$

$$\frac{dQ_g}{dz} = \frac{q_B''(W_{ch} + 2W_w)N_{ch}}{\rho_{g,in}h_{fg,in}}, \tag{12}$$

and $L_{sp,f} = \frac{GW_{ch}H_{ch}}{q_B''(W_{ch} + 2W_w)}c_{p,f}(T_{sat} - T_{b,f})_{in}.$ (13)

Fig. 8(a)–(e) capture the influences of the above parameters on average power spectrum and oscillation frequency. Increases in ΔQ_g, Fig. 8(a), and dQ_g/dz, Fig. 8(c), are shown increasing oscillation amplitude by intensifying vapor backflow to the inlet plenum. Similarly, they increase oscillation frequency almost linearly, as shown in Fig. 8(b) and (d), because of faster vapor generation that decreases waiting time for the vapor backflow. Eqs. (11) and (12) show that, in terms of vapor generation, q_B'' has the most dominant impact on both amplitude and frequency. Fig. 8(e) and (f), show that amplitude and frequency, respectively, of the oscillations generally decrease with increasing inlet subcooling, $\Delta T_{sub,in}$, due to damping of vapor backflow by increased liquid inertia and vapor-liquid mixing in the inlet plenum. Notice that, while ΔQ_g and dQ_g/dz are influenced mostly by q_B'', $L_{sp,f}$ is influenced by both q_B'' and G.

To derive a non-dimensional correlation for oscillation frequency, four dependent dimensionless parameters are defined: phase change parameter, N_{pch}, subcooling parameter, N_{sub}, single-phase length parameter, $I_{sp,f}$, and Weber number, We_{fo}. The phase change parameter is defined as

$$N_{pch} = \left(\frac{q_H''}{Gh_{fg}}\right)\left(\frac{L}{A/P_H}\right)\left(\frac{\rho_f - \rho_g}{\rho_g}\right) = Bo\left(\frac{L}{A/P_H}\right)\left(\frac{\rho_f - \rho_g}{\rho_g}\right), \tag{14}$$
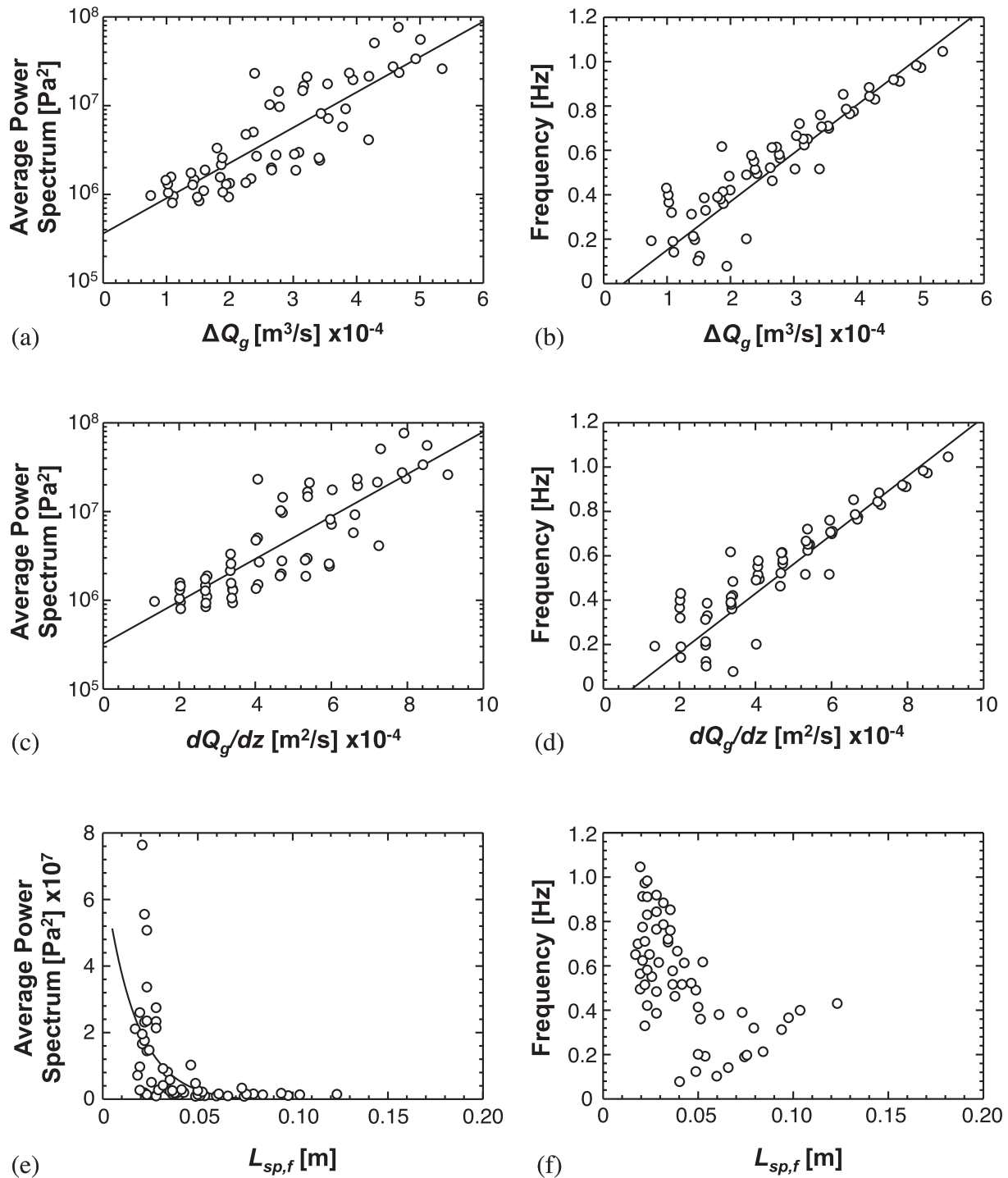
Fig. 8. Effects of vapor generation parameters on average power spectrum and frequency of pressure drop oscillations. (a) Power spectrum versus vapor volume. (b) Frequency versus vapor volume. (c) Power spectrum versus vapor generation rate. (d) Frequency versus vapor generation rate. (e) Power spectrum versus liquid length. (f) Frequency versus liquid length.

where $P_H = W_{ch} + 2H_{ch}$. The proportional dependence of N_{pch} on q_H'' is reflected in Fig. 9(a) by a monotonic increase of oscillation frequency with increasing N_{pch}. The subcooling parameter is defined by

$$N_{sub} = \left(\frac{\rho_f - \rho_g}{\rho_g}\right)\left(\frac{c_{p,f}(T_{sat} - T_{in})}{h_{fg}}\right). \tag{15}$$

Fig. 9(b) shows that increasing N_{sub} suppresses oscillation frequency, however this dependence is less clearly defined than that relative to N_{pch}, given the relatively small range of subcooling of the present experiments, 3.5–5 °C, and a corresponding N_{sub} range of 0.9–1.4. The two remaining dimensionless parameters, the single-phase length parameter, $I_{sp,f}$, and the Weber number, We_{fo}, are defined, respectively, as
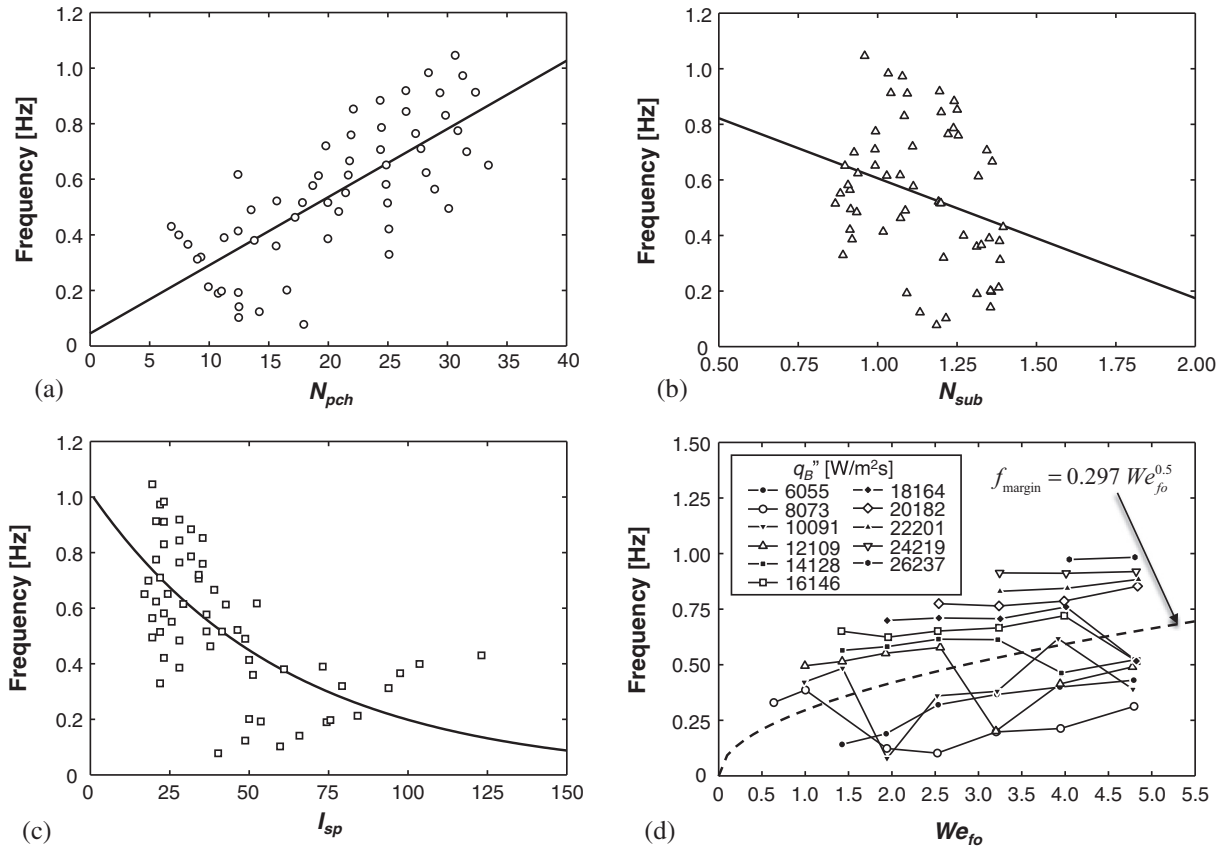
Fig. 9. Variations of oscillation frequency with (a) phase change parameter, N_{pch}, (b) subcooling parameter, N_{sub}, (c) liquid length parameter, I_{sp}, and (d) Weber number, We_{fo}.

$$I_{sp,f} = \frac{L_{sp,f}}{D_h} \tag{16}$$

and

$$We_{fo} = \frac{G^2 D_h}{\rho_f \sigma}. \tag{17}$$

Fig. 9(c) shows the frequency decays almost exponentially with increasing liquid inertia that is reflected in $I_{sp,f}$. Fig. 9(d) show two separate trends in the dependence of frequency on Weber number. For each heat flux, the frequency initially shows weak dependence on We_{fo} up to a threshold Weber number value, above which it drops sharply with increasing We_{fo}. Because Weber number represents ratio of liquid inertia to surface tension force, the threshold We_{fo} value marks a transition from high oscillation low We_{fo} range to high We_{fo} range where oscillations are suppressed by high liquid inertia. Fig. 9(d) shows the boundary between the two We_{fo} regimes fitted according to

$$f_{margin} = 0.297 \, We_{fo}^{0.5}. \tag{18}$$

4.3. New correlation for oscillation frequency

Combining the parametric trends of frequency with the individual dimensionless parameters yields the following correlation for oscillation frequency,

$$f[\text{Hz}] = 0.031 N_{pch} - 0.292 e^{-0.016 I_{sp}} - 0.211 N_{sub} + 0.112 We_{fo} - 0.039. \tag{19}$$

Fig. 10(a) and (b) show the variations of the correlation's absolute error, defined as

$$AE = \frac{|f_{pred} - f_{exp}|}{f_{exp}} \times 100 \; (\%), \tag{20}$$

with N_{pch} and N_{sub}, respectively, with the individual data segregated relative to f_{margin}. Notice the relatively large scatter in Fig. 10 (a) and (b) for $N_{pch} < 20$ and $N_{sub} > 1.1$, respectively. On the other hand, relatively small errors are achieved for $N_{pch} > 20$, with a MAE of 8.13% for 30 of 58 data points, and $N_{sub} > 1.1$, with a MAE of 11.97% for 27 of 58 data points, where

$$MAE = \sum \frac{|f_{pred} - f_{exp}|}{f_{exp}} \times 100 (\%). \tag{21}$$

Notice also that the data points associated with $f_{exp} > f_{margin}$ in Fig. 10(a) correspond well with the range $N_{pch} > 20$. On the other hand, no such correspondence is observed in Fig. 10(b) for $N_{sub} < 1.1$. Because of the better correspondence for data corresponding to $f_{exp} > f_{margin}$ in the variation relative to N_{pch}, Fig. 10(c) shows a smaller MAE of 9.98% for $f_{exp} \geq f_{margin}$ compared to a larger MAE of 52.71% for $f_{exp} < f_{margin}$. Fig. 10(c) also shows overall MAE for the entire database is 26.93%.

5. Heat transfer degradation due to intermittent dryout

5.1. Relation between pressure oscillations and intermittent dryout

As discussed earlier, two-phase flow between two plenums is known to induce periodic pressure oscillations that influence the local heat transfer coefficient, h, by promoting intermittent dryout. For a channel with large L/D_h and both low mass velocity and low heat flux, the intermittent dryout is initiated in the downstream region of the channel by annular film dryout, and is manifest by a sharp and significant drop in the local heat transfer coefficient. For a micro-channel heat sink with small L/D_h, high heat flux com-
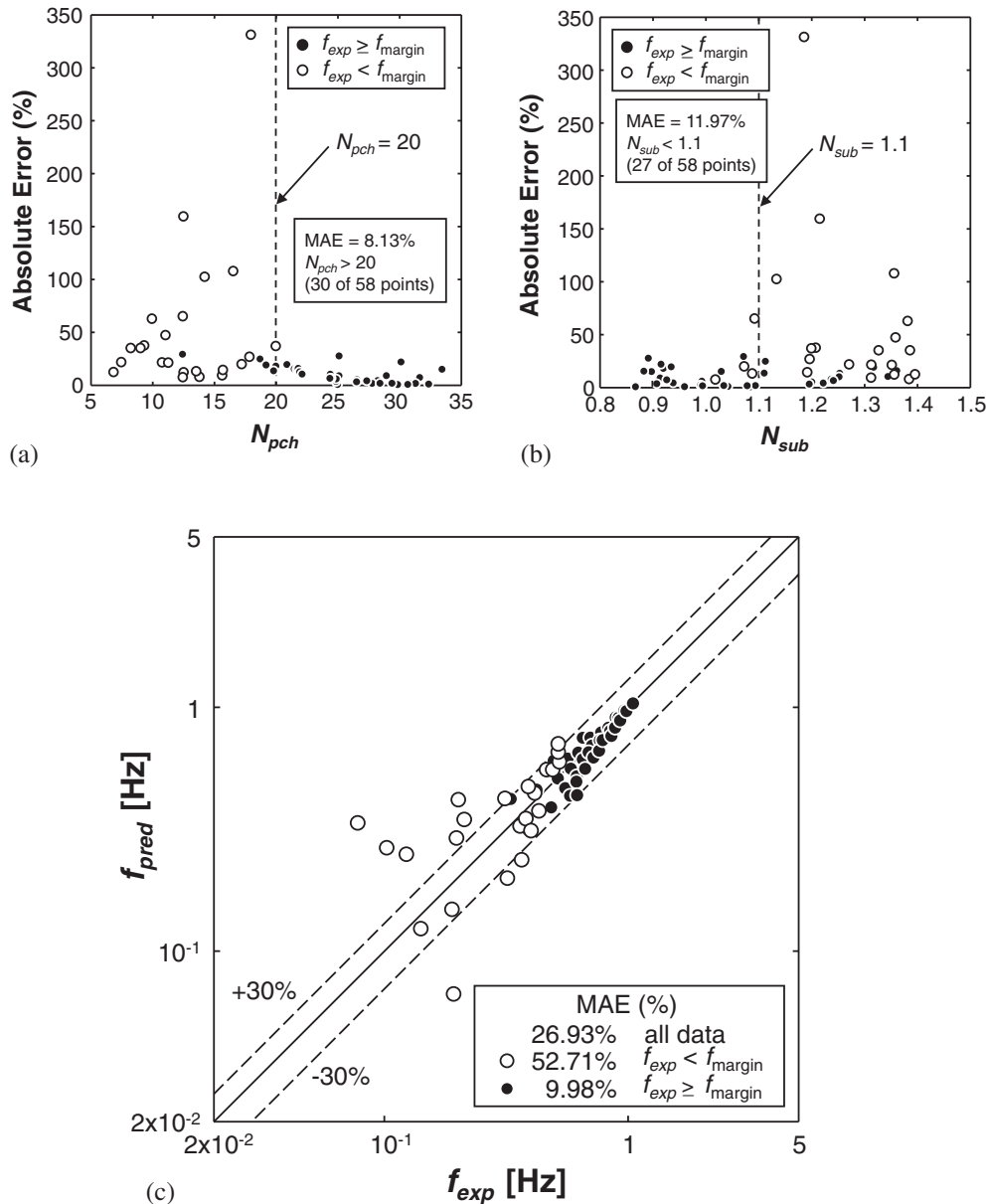
Fig. 10. Assessment of accuracy of new frequency correlation. (a) Absolute error versus N_{pch}. (b) Absolute error versus N_{sub}. (c) Predicted versus measured frequency.

bined with small mass velocity causes a reduction in the heat transfer coefficient along the entire channel by explosive boiling oscillation (EBO) because of temporal and/or complete liquid film dryout. Given the large value of L/D_h in the present study, the primary influence of pressure oscillations is localized intermittent liquid film dryout and reduction in the local heat transfer coefficient only in the downstream region of the channel.

As shown in Fig. 11(a), different trends of local heat transfer coefficient are observed in the present study, segregated by a specific Boiling number value of $Bo = q''_H/(Gh_{fg}) = 4.5 \times 10^{-4}$. In the low x_e range corresponding to $Bo < 4.5 \times 10^{-4}$, the local heat transfer coefficient increases almost linearly with increasing Bo because of intensification of boiling in a predominantly nucleate boiling region. However, h data are quite dispersed for $Bo \geq 4.5 \times 10^{-4}$, due to intermittent dryout in a predominantly convective boiling region. The segregation in local heat transfer coefficient data is emphasized further by plotting h data versus x_e separately for $Bo < 4.5 \times 10^{-4}$, Fig. 11(b), and $Bo \geq 4.5 \times 10^{-4}$, Fig. 11(c). Notice that for $Bo \geq 4.5 \times 10^{-4}$ h is simultaneously

enhanced by nucleate boiling upstream and degraded by intermittent dryout downstream, with the degradation dominating the trend relative to x_e, especially as x_e approaches unity as shown in Fig. 11(c). This trend is also supported by Fig. 11(d), which shows exit quality values above 0.8 correspond closely to the range $Bo \geq 4.5 \times 10^{-4}$. The results in Figs. 5(a)–(c) and 11(a)–(d), point to intermittent dryout and very high quality values downstream as key causes for the downstream degradation in h.

It is important to note that the pressure oscillations and vapor backflow induce the periodic flow oscillations that are responsible for the downstream intermittent dryout. It is also expected that further increases in Bo and $x_{e,out}$ due to increasing heat flux can trigger critical heat flux (CHF). Notice that this type of CHF, which occurs in saturated flow boiling, is fundamentally different from premature CHF [14], which is encountered with subcooled outlet conditions, $x_{e,out} < 0$.

To further explore the intermittent dryout phenomenon, the mean thickness of the annular liquid film incurring dryout by evaporation is estimated over period t of the flow oscillation.
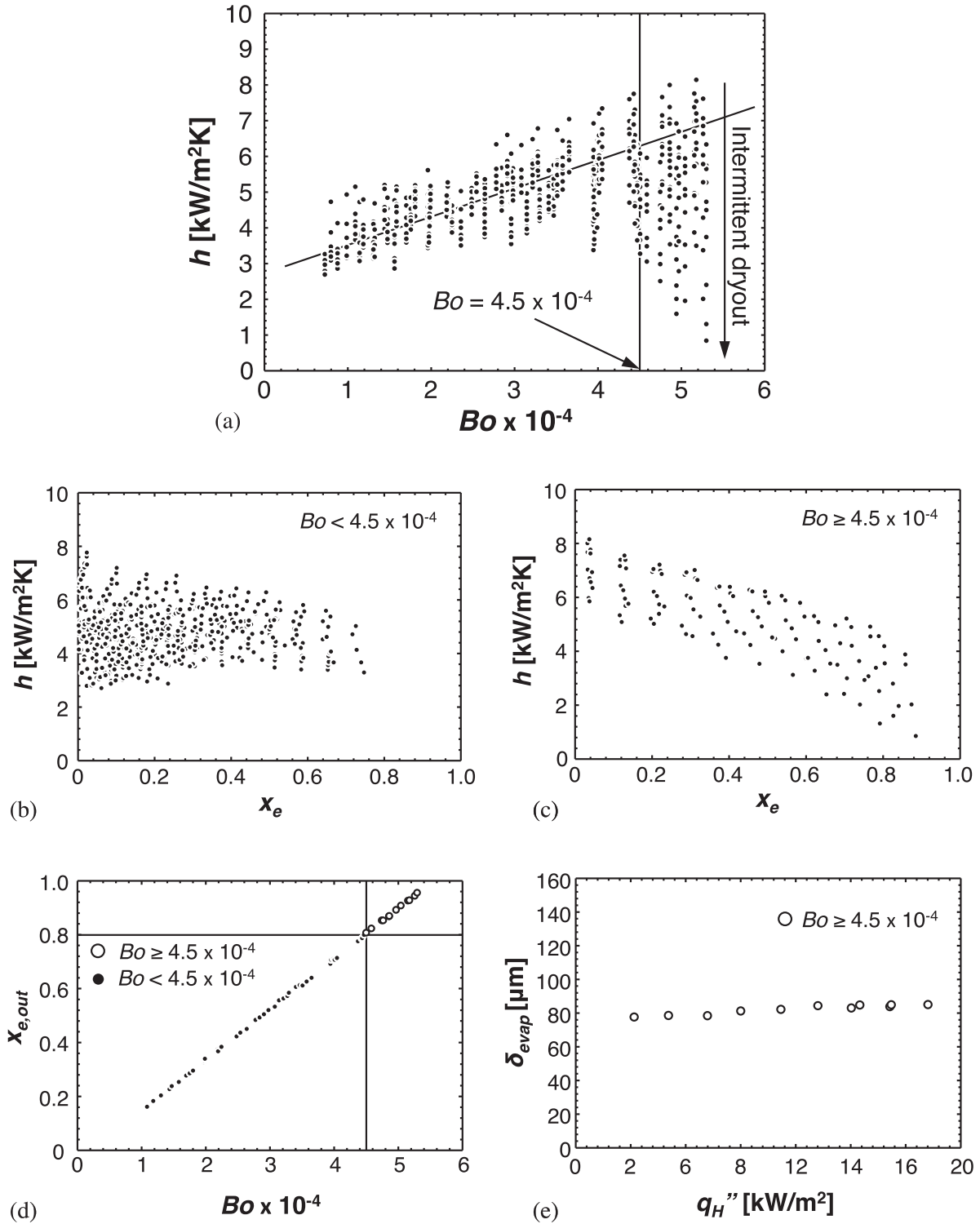
Fig. 11. Effects of pressure and flow oscillations and intermittent dryout on heat transfer degradation; data are time-averaged over 5 min after reaching steady state. (a) h versus Bo. (b) h versus $x_{e,out}$ for $Bo \geq 4.5 \times 10^{-4}$. (c) h versus $x_{e,out}$ for $Bo < 4.5 \times 10^{-4}$. (d) $x_{e,out}$ versus Bo. (e) q_H'' versus evaporating film thickness, δ_{evap}, during one oscillation cycle for $Bo \geq 4.5 \times 10^{-4}$.

$$\delta_{evap} = \frac{q_H'' t}{\rho_f h_{fg}} = \left(\frac{W_{ch} + 2W_w}{W_{ch} + 2H_{ch}}\right)\frac{q_B'' t}{\rho_f h_{fg}}. \tag{22}$$

Fig. 11(e) shows the film thickness is fairly constant, 80–100 μm, for $Bo \geq 4.5 \times 10^{-4}$ because the opposing effects of evaporation period and heat flux on film thickness tend to cancel one another.

5.2. Future work

A long-term objective of this study is to implement flow boiling and condensation in thermal control systems (TCSs) for future space vehicles and planetary habitats. These operating environments pose additional challenges stemming from influences of

reduced gravity on flow instabilities in the two-phase loop, especially the flow boiling module. For example, past studies at the Purdue University Boiling and Two-Phase Flow Laboratory (PU-BTPFL) [85–87] have shown profound changes in flow boiling interfacial behavior in microgravity, Lunar gravity, and Martian gravity compared to Earth gravity, especially at low coolant flow rates. Another concern is to ensure that recently developed predictive tools for both flow boiling [88,89] and condensation [90–92] are valid for the different gravities. Future studies must therefore address two-phase flow and heat transfer instability issues in reduced gravity, and provide, if needed, improved methods for predicting flow boiling and condensation in reduced gravity.

6. Conclusion

This study explored the complex two-phase phenomena associated with pressure oscillations in a large length-to-diameter multi micro-channel heat sink using R134a as working fluid. Vapor backflow to the upstream plenum was investigated with the aid of high-speed video and used to estimate oscillation frequency. A detailed parametric study of oscillation frequency was conducted to identify key dimensionless parameters governing the instability, and to develop a new frequency correlation. Also discussed was the influence of oscillation frequency on intermittent dryout in the downstream regions of the channels. Key findings from the study are as follows.

1. High-speed video analysis proved vapor backflow induces periodic pressure oscillations in the inlet plenum. The frequency estimated from the vapor backflow video analysis matches closely the frequency obtained from Fourier analysis of the measured pressure drop signals. While density-wave oscillations are encountered in individual channels, the phenomena observed are more closely related to parallel-channel instability.
2. The periodic oscillations and vapor backflow are responsible for initiating intermittent dryout in the downstream regions of the channels, which is manifest by an appreciable drop in the local heat transfer coefficient, especially for downstream locations where $x_{e,out} \geq 0.8$.
3. Oscillation frequency is governed by four dimensionless parameters that account for amount of vapor generation, subcooling, and upstream liquid length, in addition to Weber number. A correlation for oscillation frequency is constructed which captures the frequency variations relative to the individual parameters.

Acknowledgement

Conflict of interest

We wish to confirm that there are no known conflicts of interest.

References

[1] I. Mudawar, Assessment of high-heat-flux thermal management schemes, IEEE Trans. - CPMT 24 (2001) 122–141.
[2] C.L. Tien, K.S. Chung, Entrainment limits in heat pipes, AIAA J. 17 (1979) 643–646.
[3] M. Shafahi, V. Bianco, H. Vafai, O. Manco, An investigation of the thermal performance of cylindrical heat pipes using nanofluids, Int. J. Heat Mass Transfer 53 (2010) 376–383.
[4] T.J. LaClair, I. Mudawar, Thermal transients in a capillary evaporator prior to the initiation of boiling, Int. J. Heat Mass Transfer 43 (2000) 3937–3952.
[5] P.J. Marto, V.J. Lepere, Pool boiling heat transfer from enhanced surfaces to dielectric fluids, J. Heat Transfer 104 (1982) 292–299.
[6] I. Mudawar, T.M. Anderson, Optimization of extended surfaces for high flux chip cooling by pool boiling, J. Electronic Packaging 115 (1993) 89–100.
[7] I. Mudawar, A.H. Howard, C.O. Gersey, An analytical model for near-saturated pool boiling CHF on vertical surfaces, Int. J. Heat Mass Transfer 40 (1997) 2327–2339.
[8] J.A. Shmerler, I. Mudawar, Local heat transfer coefficient in wavy free-falling turbulent liquid films undergoing uniform sensible heating, Int. J. Heat Mass Transfer 31 (1988) 67–77.
[9] D.E. Maddox, I. Mudawar, Single- and two-phase convective heat transfer from smooth and enhanced microelectronic heat sources in a rectangular channel, in: H.R. Jacobs (Ed.), Proc. 1988 National Heat Transfer Conf., HTD-Vol. 96, Houston, Texas, 1988, pp. 533–542.
[10] T.C. Willingham, I. Mudawar, Forced-convection boiling and critical heat flux from a linear array of discrete heat sources, Int. J. Heat Mass Transfer 35 (1992) 2879–2890.
[11] C.O. Gersey, I. Mudawar, Effects of heater length and orientation on the trigger mechanism for near-saturated flow boiling CHF - I. Photographic and statistical characterization of the near-wall interfacial features, Int. J. Heat Mass Transfer 38 (1995) 629–642.
[12] J.C. Sturgis, I. Mudawar, Critical heat flux in a long, rectangular channel subjected to one-sided heating - II. Analysis of CHF data, Int. J. Heat Mass Transfer 42 (1999) 1849–1862.
[13] S.M. Ghiaasiaan, Two-Phase Flow, Boiling and Condensation in Conventional and Miniature Systems, Cambridge University Press, New York, 2008.
[14] J. Lee, I. Mudawar, Critical heat flux for subcooled flow boiling in micro-channel heat sinks, Int. J. Heat Mass Transfer 52 (2009) 3341–3352.
[15] J. Lee, I. Mudawar, Fluid flow and heat transfer characteristics of low temperature two-phase micro-channel heat sinks – part 1: Experimental methods and flow visualization results, Int. J. Heat Mass Transfer 51 (2008) 4315–4326.
[16] J.Y. Min, S.P. Jang, S.J. Kim, Effect of tip clearance on the cooling performance of a microchannel heat sink, Int. J. Heat Mass Transfer 47 (2004) 1099–1103.
[17] J.M. Koo, S. Im, L. Jiang, K.E. Goodson, integrated microchannel cooling for three-dimensional electronic circuit architectures, J. Heat Transfer 127 (2005) 49–58.
[18] I. Mudawar, M.B. Bowers, Ultra-high critical heat flux (CHF) for subcooled water flow boiling - I. CHF data and parametric effects for small diameter tubes, Int. J. Heat Mass Transfer 42 (1999) 1405–1428.
[19] D.D. Hall, I. Mudawar, Ultra-high critical heat flux (CHF) for subcooled water flow boiling - II. High-CHF database and design parameters, Int. J. Heat Mass Transfer 42 (1999) 1429–1456.
[20] S. Mukherjee, I. Mudawar, Smart pumpless loop for micro-channel electronic cooling using flat and enhanced surfaces, IEEE Trans. - CPMT 26 (2003) 99–109.
[21] M. Monde, T. Inoue, Critical heat flux in saturated forced convective boiling on a heated disk with multiple impinging jets, J. Heat Transfer 113 (1991) 722–727.
[22] D.C. Wadsworth, I. Mudawar, Enhancement of single-phase heat transfer and critical heat flux from an ultra-high-flux simulated microelectronic heat source to a rectangular impinging jet of dielectric liquid, J. Heat Transfer 114 (1992) 764–768.
[23] I. Mudawar, Recent advances in high-flux, two-phase thermal management, J. Therm. Sci. Eng. Appl. 5 (2013) 021012.
[24] D.D. Hall, I. Mudawar, Experimental and numerical study of quenching complex-shaped metallic alloys with multiple, overlapping sprays, Int. J. Heat Mass Transfer 38 (1995) 1201–1216.
[25] L. Lin, R. Ponnappan, Heat transfer characteristics of spray cooling in a closed loop, Int. J. Heat Mass Transfer 46 (2003) 3737–3746.
[26] J.D. Bernardin, I. Mudawar, A Leidenfrost point model for impinging droplets and sprays, J. Heat Transfer 126 (2004) 272–278.
[27] M. Visaria, I. Mudawar, Effects of high subcooling on two-phase spray cooling and critical heat flux, Int. J. Heat Mass Transfer 51 (2008) 5269–5278.
[28] I. Mudawar, D. Bharathan, K. Kelly, S. Narumanchi, Two-phase spray cooling of hybrid vehicle electronics, IEEE Trans. - CPMT 32 (2009) 501–512.
[29] M.K. Sung, I. Mudawar, Experimental and numerical investigation of single-phase heat transfer using a hybrid jet impingement/micro-channel cooling scheme, Int. J. Heat Mass Transfer 49 (2006) 682–694.
[30] I. Mudawar, Two-phase micro-channel heat sinks: theory, applications and limitations, J. Electronic Packaging 133 (2011) 041002–041012.
[31] M.B. Bowers, I. Mudawar, Two-phase electronic cooling using mini-channel and micro-channel heat sinks - part 2. Flow rate and pressure drop constraints, J. Electronic Packaging 116 (1994) 298–305.
[32] S.H. Lee, I. Mudawar, M.M. Hasan, Thermal analysis of hybrid single-phase, two-phase and heat pump thermal control system (TCS) for future spacecraft, Appl. Therm. Eng. 100 (2016) 190–214.
[33] S. Lin, P.A. Kew, K. Cornwell, Two-phase heat transfer to a refrigerant in a 1 mm diameter tube, Int. J. Refrigeration 24 (2001) 51–56.
[34] S. In, S. Jeong, Flow boiling heat transfer characteristics of R123 and R134a in a micro-channel, Int. J. Multiphase Flow 35 (2009) 987–1000.
[35] C.B. Tibiriçá, G. Ribatski, Flow boiling heat transfer of R134a and R245fa in a 2.3 mm tube, Int. J. Heat Mass Transfer 53 (2010) 2459–2468.

[36] M. Ducoulombier, S. Colasson, J. Bonjour, P. Haberschill, Carbon dioxide flow boiling in a single microchannel - Part II: Heat transfer, Exp. Therm. Fluid Sci. 35 (2011) 597–611.

[37] L. Wojtan, T. Ursenbacher, J.R. Thome, Investigation of flow boiling in horizontal tubes: Part I - A new diabatic two-phase flow pattern map, Int. J. Heat Mass Transfer 48 (2005) 2955–2969.

[38] R. Revellin, J.R. Thome, A new type of diabatic flow pattern map for boiling heat transfer in microchannels, J. Micromech. Microeng. 17 (2007) 788–796.

[39] S. Lee, I. Mudawar, Investigation of flow boiling in large micro-channel heat exchangers in a refrigeration loop for space applications, Int. J. Heat Mass Transfer 97 (2016) 110–129.

[40] S. Lee, I. Mudawar, Transient characteristics of flow boiling in large micro-channel heat exchangers, Int. J. Heat Mass Transfer 103 (2016) 186–202.

[41] S. Lee, I. Mudawar, Thermal and thermodynamic performance, and pressure oscillations of refrigeration loop employing large micro-channel evaporators, Int. J. Heat Mass Transfer 103 (2016) 1313–1326.

[42] J.A. Boure, A.E. Bergles, L.S. Tong, Review of two-phase flow instability, Nucl. Eng. Des. 25 (1973) 165–192.

[43] S. Kakaç, B. Bon, A Review of two-phase flow dynamic instabilities in tube boiling systems, Int. J. Heat Mass Transfer 51 (2008) 399–433.

[44] J.S. Maulbetsch, P. Griffith, A study of system-induced instabilities in forced-convection flows with subcooled boiling, Tech. Report No. 5382-35, Dept. of Mechanical Engineering, Massachusetts Institute of Technology, Cambridge, MA, 1965.

[45] T. Zhang, T. Tong, J.-Y. Chang, Y. Peles, R. Prasher, M.K. Jensen, J.T. Wen, P. Phelan, Ledinegg instability in microchannels, Int. J. Heat Mass Transfer 52 (2009) 5661–5674.

[46] K.H. Chang, C. Pan, Two-phase flow instability for boiling in a microchannel heat sink, Int. J. Heat Mass Transfer 50 (2007) 2078–2088.

[47] S. Saitoh, H. Daiguji, E. Hihara, Effect of tube diameter on boiling heat transfer of R-134a in horizontal small-diameter tubes, Int. J. Heat Mass Transfer 48 (2005) 4973–4984.

[48] P. Saha, M. Ishii, N. Zuber, An experimental investigation of the thermally induced flow oscillations in two-phase systems, J. Heat Transfer 98 (1976) 616–622.

[49] H.C. Ünal, The period of density-wave oscillations in forced convection steam generator tubes, Int. J. Heat Mass Transfer 25 (1982) 419–421.

[50] L.E. O'Neill, C.R. Kharangate, I. Mudawar, Time-averaged and transient pressure drop for flow boiling with saturated inlet conditions, Int. J. Heat Mass Transfer 103 (2016) 133–153.

[51] L.E. O'Neill, I. Mudawar, M.M. Hasan, H.K. Nahra, B. Ramaswamy, N.R. Hall, A. Lokey, J.R. Mackey, Experimental investigation into the impact of density wave oscillations on flow boiling system dynamic behavior and stability, Int. J. Heat Mass Transfer (2017) (in preparation).

[52] W. Qu, I. Mudawar, Transport phenomena in two-phase micro-channel heat sinks, J. Electronic Packaging 126 (2004) 213–224.

[53] C. Huh, J. Kim, M.H. Kim, Flow pattern transition instability during flow boiling in a single microchannel, Int. J. Heat Mass Transfer 50 (2007) 1049–1060.

[54] H.Y. Wu, P. Cheng, Visualization and measurements of periodic boiling in silicon microchannels, Int. J. Heat Mass Transfer 46 (2003) 2603–2614.

[55] T. Zhang, Y. Peles, J.T. Wen, T. Tong, J.-Y. Chang, R. Prasher, M.K. Jensen, Analysis and active control of pressure-drop flow instabilities in boiling microchannel systems, Int. J. Heat Mass Transfer 53 (2010) 2347–2360.

[56] Y. Ding, S. Kakaç, X.J. Chen, Dynamic instabilities of boiling two-phase flow in a single horizontal channel, Exp. Therm. Fluid Sci. 11 (1995) 327–342.

[57] A.H. Stenning, T.N. Veziroğlu, Flow oscillation modes in forced-convection boiling, in: Proc. 1965 Heat Transfer Fluid Mechanics Institute, Stanford University Press, pp. 301–316.

[58] A.H. Stenning, T.N. Veziroğlu, G.M. Callahan, Pressure-drop oscillations in forced convection flow with boiling, in: EURATOM Symp. Two-phase Flow Dynamics, Eindhoven, Netherlands, 1967, pp. 405–427.

[59] M. Ozawa, S. Nakanishi, S. Ishigai, Y. Mizuta, H. Tarui, Flow instabilities in boiling channels: Part 1. Pressure drop oscillation, Bull. JSME 22 (1979) 1113–1118.

[60] D. Brutin, F. Topin, L. Tadrist, Experimental study of unsteady convective boiling in heated minichannels, Int. J. Heat Mass Transfer 46 (2003) 2957–2965.

[61] P. Balasubramanian, S.G. Kandlikar, Experimental study of flow patterns, pressure drop, and flow instabilities in parallel rectangular minichannels, Heat Transfer Eng. 26 (2005) 20–27.

[62] G. Hetsroni, A. Mosyak, E. Pogrebnyak, Z. Segal, Periodic boiling in parallel micro-channels at low vapor quality, Int. J. Multiphase Flow 32 (2006) 1141–1159.

[63] K. Fukuda, S. Hasegawa, Analysis on two-phase flow instability in parallel multichannels, J. Nucl. Sci. Technol. 16 (1979) 190–199.

[64] G. Hetsroni, A. Mosyak, E. Pogrebnyak, Z. Segal, Explosive boiling of water in parallel micro-channels, Int. J. Multiphase Flow 31 (2005) 371–392.

[65] W. Qu, I. Mudawar, Measurement and correlation of critical heat flux in two-phase micro-channel heat sinks, Int. J. Heat Mass Transfer 47 (2004) 2045–2059.

[66] C.T. Lu, C. Pan, Stabilization of flow boiling in microchannel heat sinks with a diverging cross-section design, J. Micromech. Microeng. 18 (2008) 075035.

[67] R. Muwanga, I. Hassan, R. MacDonald, Characteristics of flow boiling oscillations in silicon microchannel heat sinks, J. Heat Transfer 129 (2007) 1341–1351.

[68] G. Wang, P. Cheng, A.E. Bergles, Effects of inlet/outlet configurations on flow boiling instability in parallel microchannels, Int. J. Heat Mass Transfer 51 (2008) 2267–2281.

[69] H. Tuo, P. Hrnjak, Effect of venting the periodic reverse vapor flow on the performance of a microchannel evaporator in air-conditioning systems, Int. J. Heat Mass Transfer 69 (2014) 66–76.

[70] J.R. Thome, V. Dupont, A.M. Jacobi, Heat transfer model for evaporation in microchannels. Part I: presentation of the model, Int. J. Heat Mass Transfer 47 (2004) 3375–3385.

[71] S. Szczukiewicz, N. Borhani, J.R. Thome, Two-phase heat transfer and high-speed visualization of refrigerant flows in 100×100 μm 2 silicon multi-microchannels, Int. J. Refrigeration 36 (2013) 402–413.

[72] B. Agostini, J.R. Thome, M. Fabbri, B. Michel, D. Calmi, U. Kloter, High heat flux flow boiling in silicon multi-microchannels – Part I: Heat transfer characteristics of refrigerant R236fa, Int. J. Heat Mass Transfer 51 (2008) 5400–5414.

[73] G. Hetsroni, A. Mosyak, Z. Segal, E. Pogrebnyak, Two-phase flow patterns in parallel micro-channels, Int. J. Multiphase Flow 29 (2003) 341–360.

[74] V. Dupont, J.R. Thome, A.M. Jacobi, Heat transfer model for evaporation in microchannels. Part II: comparison with the database, Int. J. Heat Mass Transfer 47 (2004) 3387–3401.

[75] D. Brutin, L. Tadrist, Pressure drop and heat transfer analysis of flow boiling in a minichannel: influence of the inlet condition on two-phase flow stability, Int. J. Heat Mass Transfer 47 (2004) 2365–2377.

[76] H. Wu, P. Cheng, Boiling instability in parallel silicon microchannels at different heat flux, Int. J. Heat Mass Transfer 47 (2004) 3631–3641.

[77] J. Xu, J. Zhou, Y. Gan, Static and dynamic flow instability of a parallel microchannel heat sink at high heat fluxes, Energy Convers. Manage. 46 (2005) 313–334.

[78] G. Wang, P. Cheng, H. Wu, Unstable and stable flow boiling in parallel microchannels and in a single microchannel, Int. J. Heat Mass Transfer 50 (2007) 4297–4310.

[79] D. Bogojevic, K. Sefiane, A. Walton, H. Lin, G. Cummins, Two-phase flow instabilities in a silicon microchannels heat sink, Int. J. Heat Fluid Flow 30 (2009) 854–867.

[80] D. Bogojevic, K. Sefiane, A. Walton, H. Lin, G. Cummins, D. Kenning, T. Karayiannis, Experimental investigation of non-uniform heating effect on flow boiling instabilities in a microchannel-based heat sink, Int. J. Therm. Sci. 50 (2011) 309–324.

[81] T.L. Bergman, F.P. Incropera, A.S. Lavine, D.P. DeWitt, Fundamentals of Heat and Mass Transfer, seventh ed., Wiley and Sons, New York, 2011.

[82] E. Kreyszig, Advanced Engineering Mathematics, ninth ed., John Wiley & Sons, New York, 2006.

[83] MATLAB, user's guide, version 6.0.088, release 12, The Mathworks inc., 2000.

[84] M.S. Plesset, S.A. Zwick, The growth of vapor bubbles in superheated liquids, J. Appl. Phys. 25 (1954) 493–500.

[85] H. Zhang, I. Mudawar, M.M. Hasan, Experimental assessment of the effects of body force, surface tension force, and inertia on flow boiling CHF, Int. J. Heat Mass Transfer 45 (2002) 4079–4095.

[86] H. Zhang, I. Mudawar, M.M. Hasan, Flow boiling CHF in microgravity, Int. J. Heat Mass Transfer 48 (2005) 3107–3118.

[87] H. Zhang, I. Mudawar, M.M. Hasan, CHF model for subcooled flow boiling in Earth gravity and microgravity, Int. J. Heat Mass Transfer 50 (2007) 4039–4051.

[88] S.M. Kim, I. Mudawar, Universal approach to predicting saturated flow boiling heat transfer in mini/micro-channels – part II. Two-phase heat transfer coefficient, Int. J. Heat Mass Transfer 64 (2013) 1239–1256.

[89] S.-M. Kim, I. Mudawar, Universal approach to predicting two-phase frictional pressure drop for mini/micro-channel saturated flow boiling, Int. J. Heat and Mass Transfer 58 (2013) 718–734.

[90] S.M. Kim, I. Mudawar, Universal approach to predicting heat transfer coefficient for condensing mini/micro-channel flow, Int. J. Heat Mass Transfer 56 (2013) 238–250.

[91] S.M. Kim, J. Kim, I. Mudawar, Flow condensation in parallel micro-channels – Part 1. Experimental results and assessment of pressure drop correlations, Int. J. Heat Mass Transfer 55 (2012) 971–983.

[92] S.M. Kim, I. Mudawar, Flow condensation in parallel micro-channels – Part 2. Heat transfer results and correlation technique, Int. J. Heat Mass Transfer 55 (2012) 984–994.